Journal of Structural Geology 104 (2017) 142–158

Contents lists available at ScienceDirect

Journal of Structural Geology

journal homepage: www.elsevier.com/locate/jsg

The effect of offset on fracture permeability of rocks from the Southern Andes Volcanic Zone, Chile

P. Pérez-Flores[a,b,*], G. Wang[c], T.M. Mitchell[d], P.G. Meredith[d], Y. Nara[e], V. Sarkar[f], J. Cembrano[a,b]

[a] Pontificia Universidad Católica de Chile, Santiago, Chile
[b] Andean Geothermal Center of Excellence (CEGA, FONDAP-CONICYT), Santiago, Chile
[c] School of Geosciences, China University of Petroleum, Qingdao, China
[d] Department of Earth Sciences, University College London, London, UK
[e] Graduate School of Engineering, Kyoto University, Kyoto, Japan
[f] Indian School of Mines, Dhanbad, India

ARTICLE INFO

Keywords:
Crustal permeability
Fractures roughness
Liquiñe-Ofqui Fault System
Offset macro-fractures

ABSTRACT

The Southern Andes Volcanic Zone (SVZ) represents one of the largest undeveloped geothermal provinces in the world. Development of the geothermal potential requires a detailed understanding of fluid transport properties of its main lithologies. The permeability of SVZ rocks is altered by the presence of fracture damage zones produced by the Liquiñe-Ofqui Fault System (LOFS) and the Andean Transverse Faults (ATF). We have therefore measured the permeability of four representative lithologies from the volcanic basement in this area: crystalline tuff, andesitic dike, altered andesite and granodiorite. For comparative purposes, we have also measured the permeability of samples of Seljadalur basalt, an Icelandic rock with widely studied and reported hydraulic properties. Specifically, we present the results of a systematic study of the effect of fractures and fracture offsets on permeability as a function of increasing effective pressure. Baseline measurements on intact samples of SVZ rocks show that the granodiorite has a permeability (10^{-18} m^2), two orders of magnitude higher than that of the volcanic rocks (10^{-20} m^2). The presence of throughgoing mated macro-fractures increases permeability by between four and six orders of magnitude, with the highest permeability recorded for the crystalline tuff. Increasing fracture offset to produce unmated fractures results in large increases in permeability up to some characteristic value of offset, beyond which permeability changes only marginally. The increase in permeability with offset appears to depend on fracture roughness and aperture, and these are different for each lithology. Overall, fractured SVZ rocks with finite offsets record permeability values consistent with those commonly found in geothermal reservoirs ($> 10^{-16}$ m^2), which potentially allow convective/advective flow to develop. Hence, our results demonstrate that the fracture damage zones developed within the SVZ produce permeable regions, especially within the transtensional NE-striking fault zones, that have major importance for geothermal energy resource potential.

1. Introduction

Understanding the influence of fractures on the hydraulic properties of rocks is key to many fundamental and applied areas of geoscience, such as deformation and faulting (Barton et al., 1995; Evans et al., 1997), geophysical hazards (e.g. Scholz and Gupta, 2000), geothermal energy recovery (e.g. Meixner et al., 2016; Rowland and Sibson, 2004), genesis of ore deposits (e.g. Cox, 1999; Liotta et al., 2015; Micklethwaite et al., 2010) and subsurface storage of oils and gas (e.g. Gudmundsson et al., 2012, 2010). In crystalline rocks, geo-fluids are primarily stored within and migrate through fault-fracture networks at all scales (Cox, 2007; Curewitz and Karson, 1997; Uehara and Shimamoto, 2004; Walker et al., 2013; Zhang and Tullis, 1998; Zucchi et al., 2017). Since fractures serve as the main pathways for fluid flow, any change in fracture properties will result in a concomitant change in rock hydraulic properties. It is therefore essential to quantify how fractures influence rock permeability, and how their effect varies with elevated pressure at depth.

Fault zones accommodate most displacement in their cores, while simultaneously developing a variety of surrounding damage zone geometries defined by fractures at all scales, from micro-fractures to macro-fractures (Kim et al., 2004; Mitchell and Faulkner, 2009). Permeability in such damage zones is enhanced by the hydraulic properties of the fault-fracture network (Caine et al., 2010, 1996; Faulkner et al., 2010;

* Corresponding author. Pontificia Universidad Catolica de Chile, Departamento de Ingenieria Estructural y Geotecnica, Santiago, Chile.
E-mail address: pvperez1@uc.cl (P. Pérez-Flores).

http://dx.doi.org/10.1016/j.jsg.2017.09.015
Received 3 May 2017; Received in revised form 16 September 2017; Accepted 29 September 2017
Available online 29 September 2017

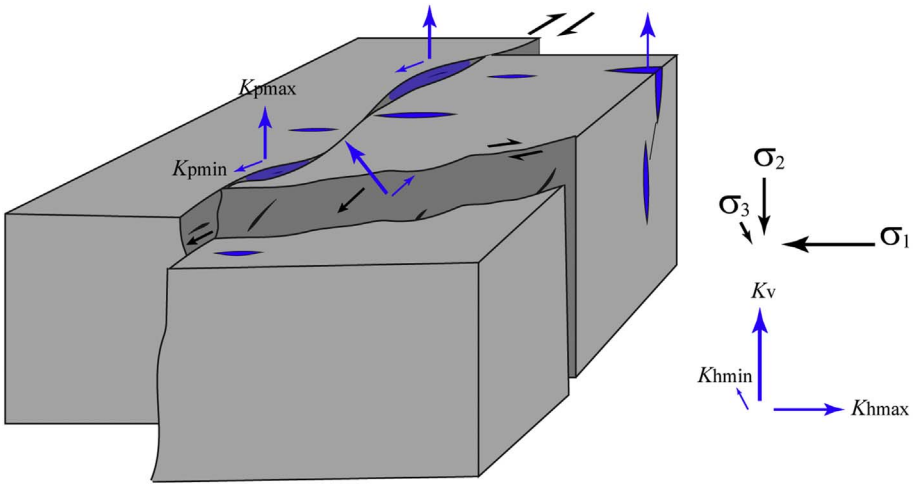

Fig. 1. Schematic diagram of a primary dextral strike-slip fault and a secondary normal-dextral fault showing the slip directions (black arrows), the maximum and minimum permeability within the fault plane (K_{pmax} and K_{pmin}, respectively; blue arrows), and kinematically associated extension fractures (in blue). The stress (σ_1- σ_2- σ_3) and permeability (K_y- K_{hmin}- K_{hmax}) tensors are also shown. (after Faulkner and Armitage, 2013). (For interpretation of the references to colour in this figure legend, the reader is referred to the web version of this article.)

Mitchell and Faulkner, 2012; Sibson, 1996), where macro-fractures dominate permeability at low effective pressure (shallow depth), but are closed more easily at higher pressure so that the microfracture networks becomes more dominant (Lamur et al., 2017; Mitchell and Faulkner, 2012; Nara et al., 2011; Wang et al., 2016). However, most studies to date have only considered mated fractures (i.e., fractures with zero offset), whereas the majority of faults found in nature are unmated and offset (Bistacchi et al., 2011; Candela et al., 2012, 2009; Griffith et al., 2010; Sagy et al., 2007). Under these latter circumstances, the fluid flow direction is controlled by the orientation of the global stress field, where the maximum permeability is parallel to the σ_2 axis (Fig. 1) (Faulkner and Armitage, 2013; Rowland and Sibson, 2004; Sibson, 1996), for all faults with the possible exception of low-angle normal faults (Brogi and Novellino, 2015). Within a fault plane the minimum permeability direction is parallel to the slip direction and perpendicular to the σ_2 axis (Fig. 1). In this context, fault slip induces dilation/opening controlled by the fault roughness (Fig. 1), thus allowing the occurrence of the flow channelling phenomenon which increases permeability by concentrating fluid flow through connected shear fractures even under high confining pressure (Min et al., 2004; Nishiyama et al., 2014; Olsson and Barton, 2001; Olsson and Brown, 1993; Raven and Gale, 1985; Walsh and Grosenbaugh, 1979; Watanabe et al., 2008). Under these circumstances, permeability increases rapidly during initial shear displacement, but then changes more gradually or reaches steady-state with increasing shear displacement (Esaki et al., 1999), where gouge production reduces permeability by several orders of magnitude with respect to the unfilled fracture (Faulkner and Rutter, 1998; Mohanty and Hsiung, 2011; Nara et al., 2013; Wang et al., 2016). Furthermore, dilational jogs and extension fractures at the tips of individual faults and/or fault intersections provide locations where stress concentrates, which leads to fault reactivation and re-opening, so that they also become the most common locations for hydrothermal outflow (Curewitz and Karson, 1997; Rowland and Sibson, 2004; Zhang et al., 2008).

In this study, we focus on basement rocks from the Southern Andes Volcanic Zone (SVZ) (Fig. 2). The SVZ represents one of the largest undeveloped geothermal provinces in the world, with an estimated potential of up to ~16,000 MW (Aravena et al., 2016; Lahsen et al., 2015a, 2015b; Sanchez-Alfaro et al., 2016). In recent years there has been significant progress in unravelling the architecture and tectonic behaviour of intra-arc fault systems in the SVZ, as well as their role in controlling migration and storage of magma and hydrothermal fluids, from a geometric and kinematic perspective (Arancibia et al., 1999; e.g. Cembrano et al., 1996; Cembrano and Lara, 2009; Lara et al., 2006, 2008; Legrand et al., 2011; Pérez-Flores et al., 2016; Rosenau et al., 2006; Sánchez et al., 2013; Sielfeld et al., 2016; Tardani et al., 2016). However, we still have no quantitative knowledge of how displacement and offset within the fault-fracture network may influence permeability in SVZ rocks.

Therefore, in order to improve our understanding of how unmated fractures control permeability as a function of depth, we measured the permeability of macro-fractured rock samples from the main basement lithologies of this volcanic province as a function of both offset and effective pressure. In summary, in the present study, we analyze how permeability varies with increasing effective pressure in (i) intact samples, (ii) samples with mated macro-fractures, and (iii) samples with unmated macro-fractures where we varied the amount of fracture offset (and, hence, also the fracture aperture).

2. Geological setting

The deformation imposed by oblique convergence between the Nazca and South America plates (Fig. 2a) is partitioned through the overriding plate within the trench, fore-arc, intra-arc, and back-arc zones. The intra-arc zone accommodates dextral transpressional strike-slip-dominated deformation, from regional to local-scale, by a series of fault-fracture networks, which are related to both the intra-arc Liquiñe-Ofqui Fault System (LOFS) and the Andean Transverse Faults (ATF) (Fig. 2a) (Cembrano and Lara, 2009; Melnick et al., 2006; Pérez-Flores et al., 2016). The LOFS includes a series of kilometric-scale, subvertical NNE-striking master faults, subvertical NE-striking secondary faults and third order ENE-to-EW-striking faults, all cropping out from the area around Callaqui volcano to ~1200 km south in the Golfo de Penas area (Fig. 2a) (e.g. Cembrano et al., 2000; Lange et al., 2008; Veloso et al., 2009).

The study area from which all our SVF sample material was collected is located between 38° and 39°S (Fig. 2b). Here, deformation is distributed within the intra-arc fault-fracture networks of both LOFS and the ATF (Pérez-Flores et al., 2016). These faults crosscut mainly volcano-sedimentary rocks belonging to the Cura-Mallin Formation (with whole rock K-Ar ages of 9–12 Ma) and the Vizcacha-Cumilao Formation (Upper Cretaceous-Paleogene), and intrusive rocks from Upper Jurassic to Miocene age (Suárez and Emparan, 1997), which are predominant south of 39°S (Llaima volcano).

The LOFS records a transpressional tectonic regime with N60E-trending σ_1 and N30W-trending σ_3, while displaying a predominant dextral to dextral-reverse slip within subvertical NNE-striking faults, dextral-normal slip within the NE- ENE-striking faults and NE-striking extensional fractures (e.g. Lavenu and Cembrano, 1999; Pérez-Flores et al., 2016; Rosenau et al., 2006). The ATF includes a series of steeply-dipping NW-striking faults, most likely inherited from a pre-Andean architecture (e.g. Radic, 2010), with sinistral-reverse kinematics and

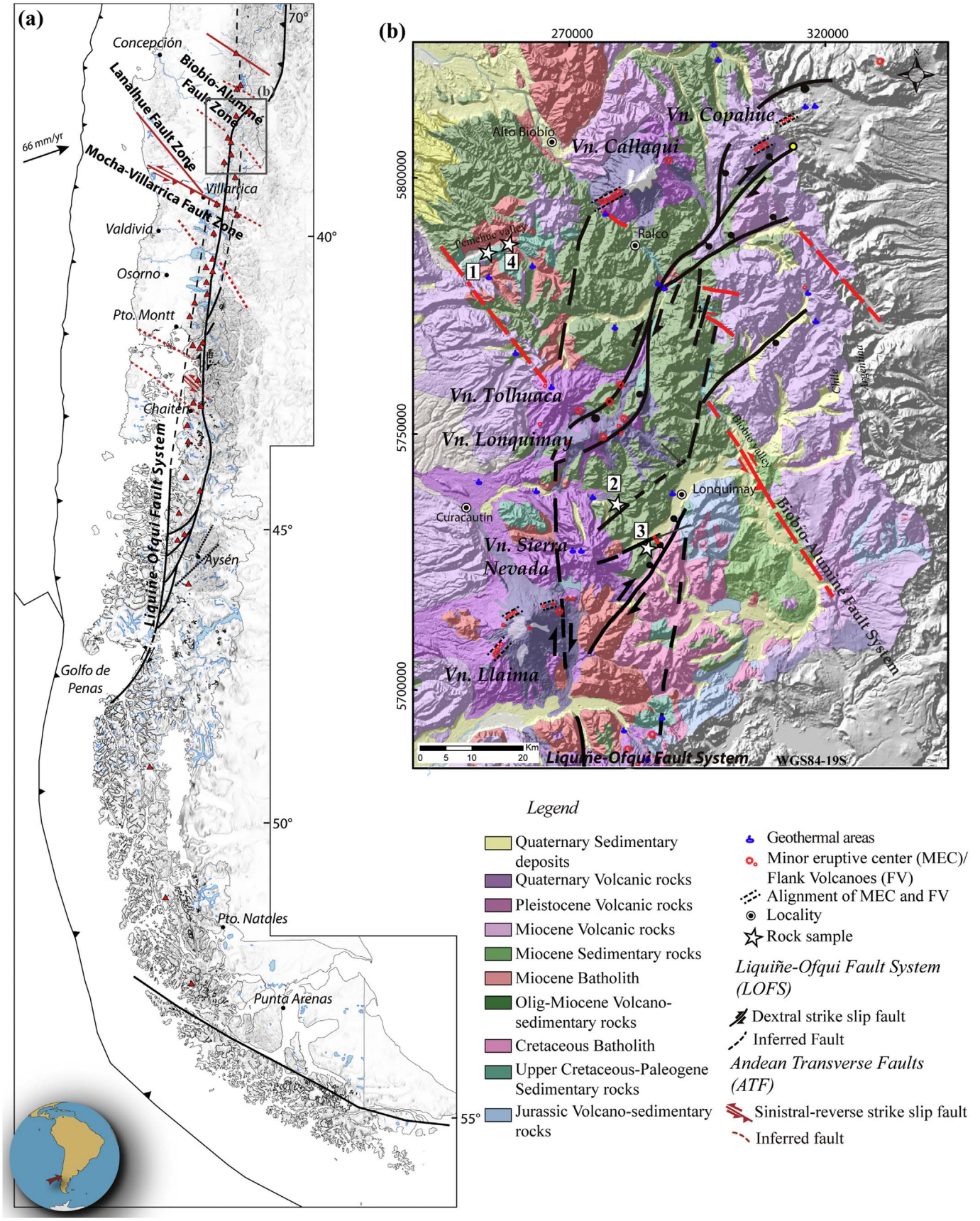

Fig. 2. (a) Structural map of the Southern Andes Volcanic Zone (SVZ), showing the trench and convergence vector of 66 mm/yr (Angermann et al., 1999). Right lateral Liquiñe-Ofqui Fault System (LOFS) (black lines), Andean Transverse Faults (ATF) (red lines), spatially and genetically associated volcanoes (red triangles) are also shown (b) Geological-structural map of the SVZ, between 37°30′S and 39°S, showing the northern termination of the LOFS, the NW-striking faults belonging to ATF (red lines) (Pérez-Flores et al., 2016), and the locations of rock samples collection sites (white stars): (1) crystalline tuff, (2) andesitic dike, (3) altered andesite and (4) granodiorite. (For interpretation of the references to colour in this figure legend, the reader is referred to the web version of this article.)

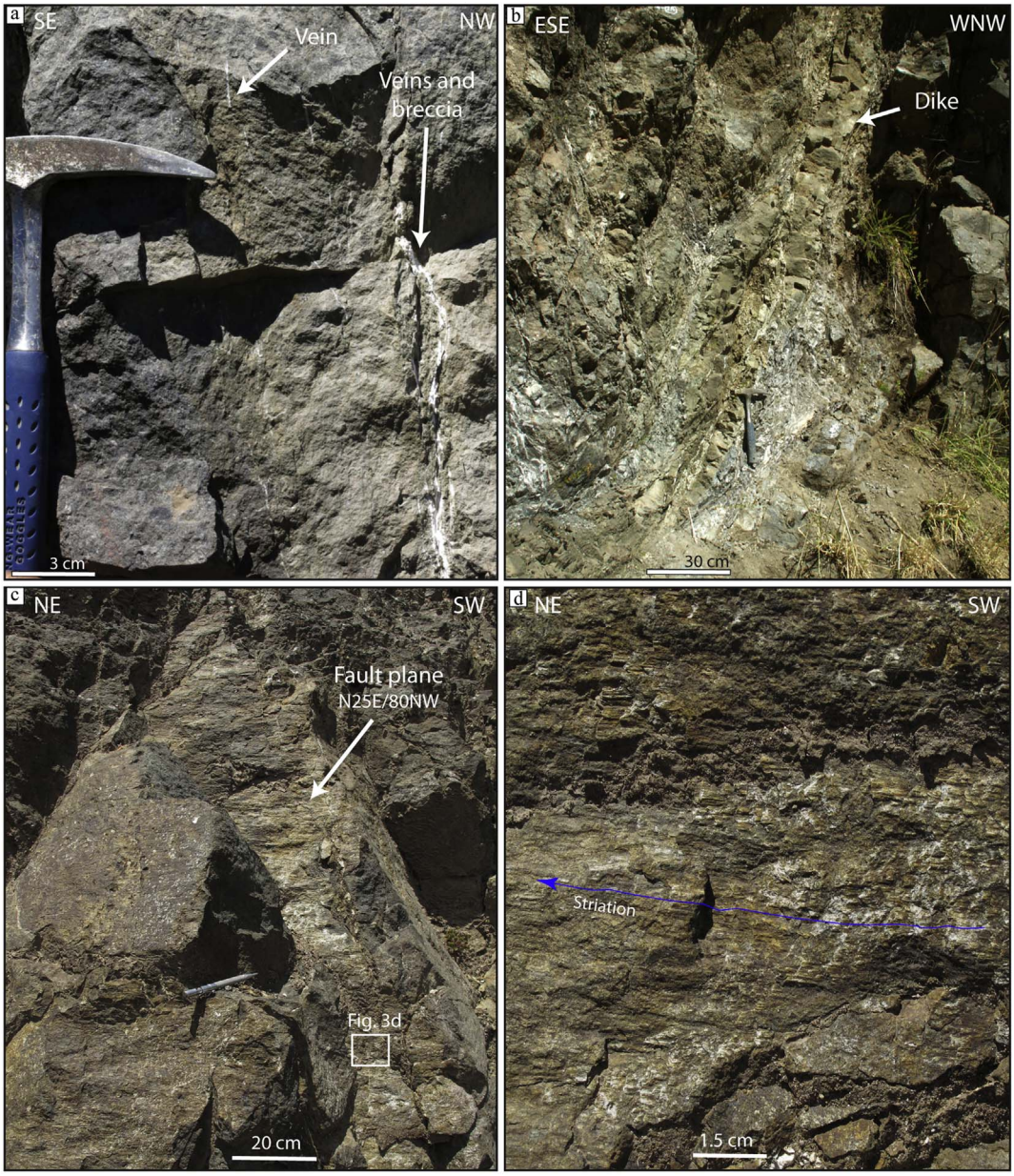

Fig. 3. Photographs of rock sample collection outcrops: (a) altered andesite crosscut by fractures and zeolite veins, (b) NE-striking fault zone-hosted andesitic dike, zeolite-calcite veins, and hydrothermal breccia, (c) NE-striking fault crosscutting altered andesite, and (d) detail of fault plane from (c) showing rough surface along the slip direction (i.e. striation) denoted by a blue line. (For interpretation of the references to colour in this figure legend, the reader is referred to the web version of this article.)

local normal-slip re-activation (Pérez-Flores et al., 2016). These fault systems are spatially and genetically associated with major strato-volcanoes (e.g. Callaqui, Llaima, Lonquimay, Tolhuaca), hot springs and with shallow earthquakes (Fig. 2) (Barrientos and Acevedo-Aránguiz, 1992; Lange et al., 2008; Legrand et al., 2011). The NE-ENE-striking fault fracture networks are favourably oriented with respect to the regional stress field for their aperture (parallel to σ_1), promoting extensional/hybrid fracturing and vertical magma/hydrothermal fluid migration (Cembrano and Lara, 2009; Pérez-Flores et al., 2016; Sielfeld et al., 2016). These fault-fracture networks record a long history of magma and hydrothermal fluid pathways, as revealed by veins (Fig. 3a), dikes (Fig. 3b) and hydrothermal breccia emplaced within these fault zones (Cembrano and Lara, 2009; Lara et al., 2008; Pérez-Flores et al., 2016; Sielfeld et al., 2016). Conversely, the NW-striking fault fracture networks are misoriented with respect to the regional stress field, favouring magma residence and hydrothermal fluid storage (Pérez-Flores et al., 2016; Sánchez et al., 2013). Fault planes consist of rough surfaces, commonly with multiple steps and slickenfibers (Fig. 3c; d). The interseismic slip rate of the LOFS, calculated from boundary element models is between 1 and 7 mm/yr, whereas the maximum slip rate calculated for NW-striking faults is 1.4 mm/yr (Stanton-Yonge et al., 2016). This tectonic context provides suitable conditions for both storage and migraton of geo-fluids, accommodated by the interaction of these fault-fracture networks (Pérez-Flores et al., 2016; Roquer et al., 2017; Sánchez et al., 2013).

3. Materials and methods

3.1. Sample materials

Permeability measurements were made on samples of five lithologies. Four of these consist of representative rock types from the volcanic basement of the SVZ, which provides the host lithologies of the intra-arc LOFS and ATF (Fig. 2b): (1) crystalline tuff, (2) andesite dike, (3)

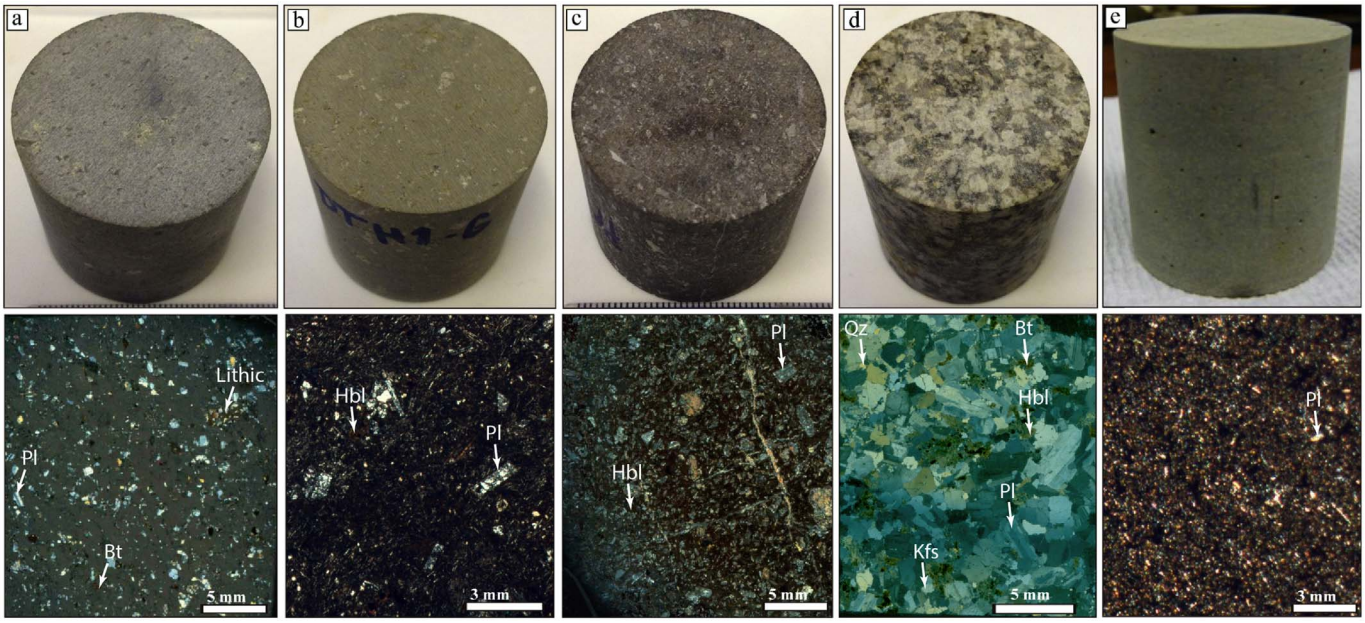

Fig. 4. Prepared intact cylindrical test samples (38 mm in diameter) and thin section images (cross polarized light) of the five lithologies used in this study: (a) crystalline tuff, (b) andesite dike, (c) altered andesite, (d) granodiorite, and (e) Seljadalur basalt. Granodiorite thin section (d) is thicker than normal, hence colors are according to increased thickness. For mineral abbreviations, see captions of Table 1. (For interpretation of the references to colour in this figure legend, the reader is referred to the web version of this article.)

altered andesite and (4) granodiorite (Fig. 4). For purposes of comparison and calibration, we also made complementary permeability measurements on samples of Seljadalur basalt (SB) from Iceland; a material that has been extensively studied previously (Benson et al., 2006b; Nara et al., 2011; Wang et al., 2016). The crystalline tuff has a pyroclastic fragmental texture comprising broken crystals of plagioclase and pyroxene, with lithic fragments and glass. This material has a moderate to highly developed clay alteration (Fig. 4a). The andesitic dike material has a porphyritic texture, and comprises primarily plagioclase and pyroxene, with a smaller quantity of hornblende phenocrysts, within a micro-crystalline matrix (Fig. 4b). The altered andesite is a porphyritic, amygdaloidal volcanic rock comprising plagioclase and pyroxene, within the same micro-crystalline matrix as the andesitic dike. Both crystallites and matrix have been subjected to moderate albitization, resulting in the presence of zeolites and clay minerals. The altered andesite exhibits narrow zeolite veins (< 1 mm) and celadonite/smectite amygdales (Fig. 4c) (Vicencio, 2015). The granodiorite has a phaneritic texture, and comprises plagioclase feldspar, quartz, hornblende, K-feldspar, and sparse biotite. This material exhibits a low level of clay alteration and contains fine quartz veins (< 1 mm) (Fig. 4d). The Seljadalur basalt (SB) comprises plagioclase feldspar and pyroxene, with some accessory minerals, in a glassy matrix (Fig. 4e). SB is a compact, high-density rock with a porosity of 3–4% and an intact matrix permeability in the range of 10^{-20} m^2 (Eccles et al., 2005; Nara et al., 2011).

Cylindrical test samples were cored from a single block of each lithology, obtained from surface outcrops. The core samples were 38 mm in diameter and 38 mm in length. Their end surfaces were ground flat and parallel to within ± 0.02 mm using a surface grinder (Fig. 4).

3.2. Permeameter and permeability measurement methodology

All permeability measurements were made in a servo-controlled permeameter using the steady-state flow method (e.g. Song et al., 2004). The apparatus (Fig. 5) and methodology are the same as those used by Nara et al. (2011). The permeameter comprises a 100 MPa hydrostatic pressure vessel equipped with dual 70 MPa servo-controlled pore fluid intensifiers. The samples are encased in rubber-jackets and positioned inside the pressure vessel between two stainless steel end-caps. The end-caps contain ports to allow pore fluid to be introduced and distributed across one end of the sample, and to be received and expelled at the other end (Benson et al., 2006a; Nara et al., 2011).

During measurements, the upstream and downstream pore fluid intensifiers are set to slightly different control pressures to maintain a small but constant pore pressure difference across the sample, thus inducing fluid flow. Once steady-state flow is established, the permeability is determined from the rate of fluid flow, the pressure gradient, and the sample dimensions via direct application of Darcy's Law. To minimize any potential temperature-induced pressure fluctuations, the apparatus is located within a temperature-controlled laboratory. The temperature was kept constant at 20 °C during all experiments.

To analyze our data, we used the simple effective pressure law, $P_{eff} = P_c - \alpha P_p$, with $\alpha = 1$, where P_c is the applied confining pressure, P_p is the mean pore-fluid pressure and P_{eff} is the effective pressure. We varied the effective pressure, P_{eff}, during our experiments by holding the mean pore fluid pressure constant at 4 MPa, and increasing the confining pressure in a series of 5 or 10 MPa steps from 9 to 64 MPa.

3.3. Experimental protocol

In order to explore systematically the effect of fracture offset on permeability, we performed four sets of experiments; (1) baseline permeability measurements on intact samples (2) measurements on samples with mated (zero offset) macro-fractures, (3) measurements on macro-fractured samples with different fracture offsets, and (4) measurements on samples with macro-fractures filled with synthetic fault gouge. The baseline permeability measurements were made on intact samples of all five lithologies under an effective pressure (P_{eff}) of 5 MPa, obtained by applying a confining pressure of 9 MPa and a mean pore fluid pressure of 4 MPa. We then introduced axial macro-fractures into several initially intact samples by loading them across their diameter using a modified Brazil test apparatus at a displacement rate of 4×10^{-6} m s^{-1} (Fig. 6), using the same methodology as that described in Nara et al. (2011). The two halves of each macro-fractured sample were then placed together before being positioned in the permeameter, with great care being taken to ensure that the macro-fractures were fully mated with no shear offset (Nara et al., 2011). We then measured the permeability of the macro-fractured samples at effective pressures

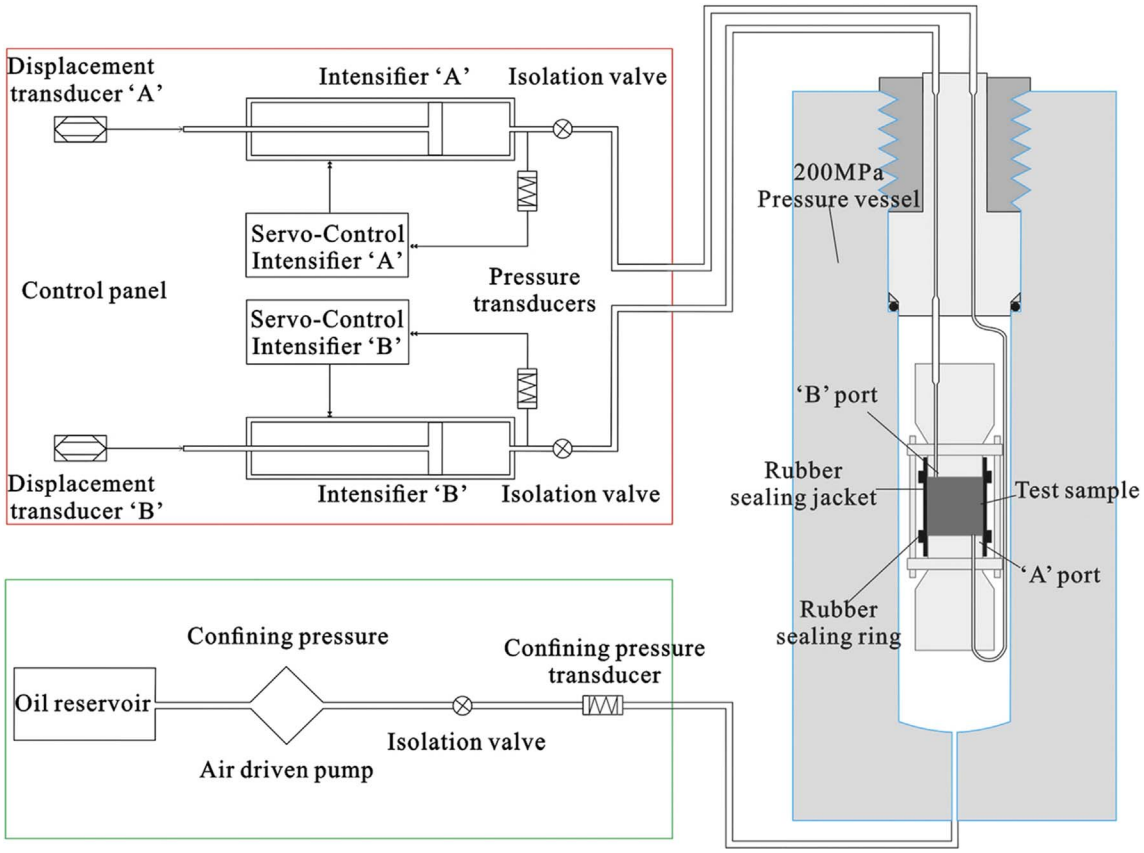

Fig. 5. Schematic diagram of the permeameter used for all permeability measurements in this study (after Nara et al., 2011; Wang et al., 2016).

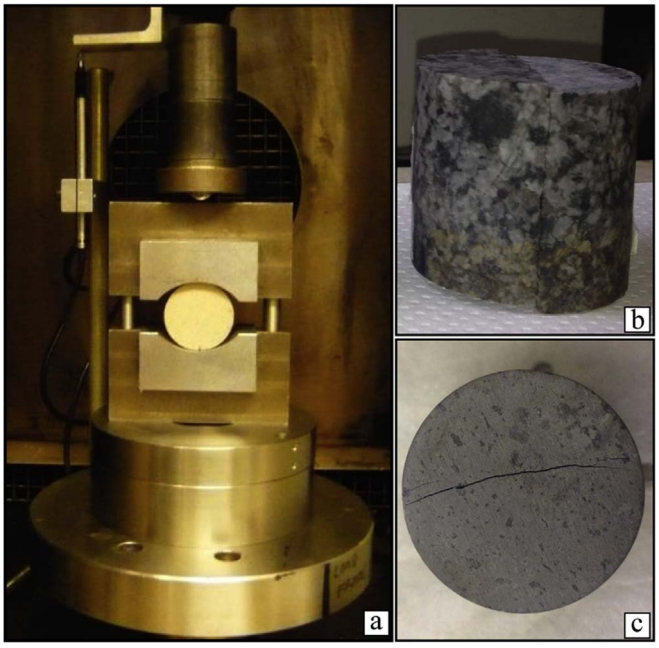

Fig. 6. (a) Modified Brazil disk apparatus for producing macro-fractured samples, (b) elevation view of macro-fractured sample of granodiorite, and (c) plan view of macro-fractured sample of crystalline tuff.

from 5 to 60 MPa.

For the third set of experiments, we manufactured samples with offset (i.e. unmated) macro-fractures. We first produced macro-fractured samples as described above (Fig. 6), and then ground the desired offset length (L_{off}) from the opposite ends of the two previously mated half samples (Fig. 7b and c). The two reduced sample halves were then placed together with their re-ground faces aligned to produce unmated, macro-fractured samples with the desired offset (L_{off}) (Fig. 7d). We made samples with values of L_{off} ranging from 0.25 to 2.00 mm. We again measured the permeability of our offset samples over the same range of effective pressure conditions as for the samples with mated fractures.

Finally, for the fourth set of experiments, we manufactured a set of macro-fractured basalt samples and filled the fractures with synthetic fault gouge made from the same material. The gouge production and fracture filling technique was identical to that described in Wang et al. (2016). We then used the gouge-filled samples to measure changes in permeability as a function of fracture offset and gouge thickness, using the same methodology and over the same effective pressure range of 5–60 MPa.

4. Results

4.1. Permeability of intact and macro-fractured SVZ rocks

The permeability of intact samples of all four lithologies from the SVZ are shown in Fig. 8, together with the change in permeability as a function of increasing effective pressure for samples of the same four rocks with mated macro-fractures. The permeability of intact SVZ samples are all low, and range from around 10^{-18} m^2 for the granodiorite to around 10^{-20} m^2 for the crystalline tuff and the andesitic dike. The presence of a macro-fracture increases the permeability by between about 5 and 7 orders of magnitude at the lowest effective pressure of 5 MPa. The largest increase is seen for the crystalline tuff, which had the lowest intact permeability, and the smallest increase is seen for the granodiorite, which had the highest intact permeability. For all four materials, the fracture permeability decreases markedly

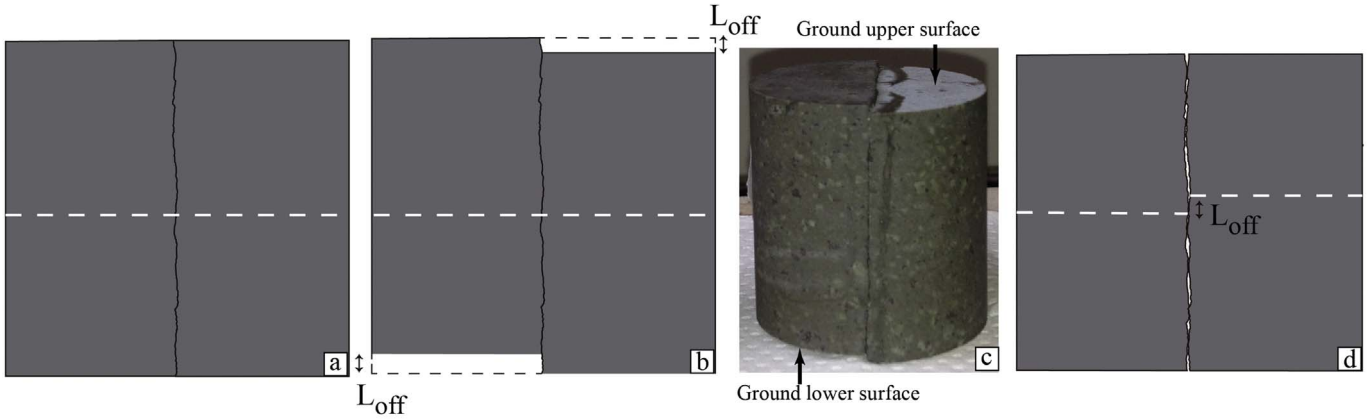

Fig. 7. Schematic diagram illustrating the methodology used to prepare controlled offsets in previously macro-fractured samples; (a) shows the original sample with a mated macro-fracture; (b) and (c) show, respectively, a diagram and photograph of the same sample with the offset dimension (L_{off}) ground off the opposite ends of the two sample halves; and (d) shows the final test sample with an unmated fracture of controlled offset produced by re-aligning the ground end-faces of the two halves.

with increasing effective pressure; dropping about three orders of magnitude as effective pressure is increased from 5 to 60 MPa.

4.2. Permeability of macro-fractured SVZ rocks as a function of fracture offset

The permeability of SVZ rock samples as functions of offset and effective pressure are shown in Fig. 9, plotted on both logarithmic and linear scales. Unsurprisingly, the permeability increases for all rock types and all effective pressures as offset is first increased from zero (mated fractures) and fractures become unmated. Again unsurprisingly, this increase is most marked at the highest effective pressure where the permeability of mated fractures was lowest. However, the pattern of permeability change becomes more complicated with increasing offset. As for mated fractures, the permeability decreases as a function of effective pressure for all lithologies and all offsets. However, the decreases are much smaller than for mated fractures, being less than one order of magnitude for the crystalline tuff, altered andesite and granodiorite, and having a maximum decrease of around two orders of magnitude for the andesite dike.

The highest permeabilities are recorded at the smallest offset of 0.25 mm for all lithologies (Fig. 9), with permeability generally

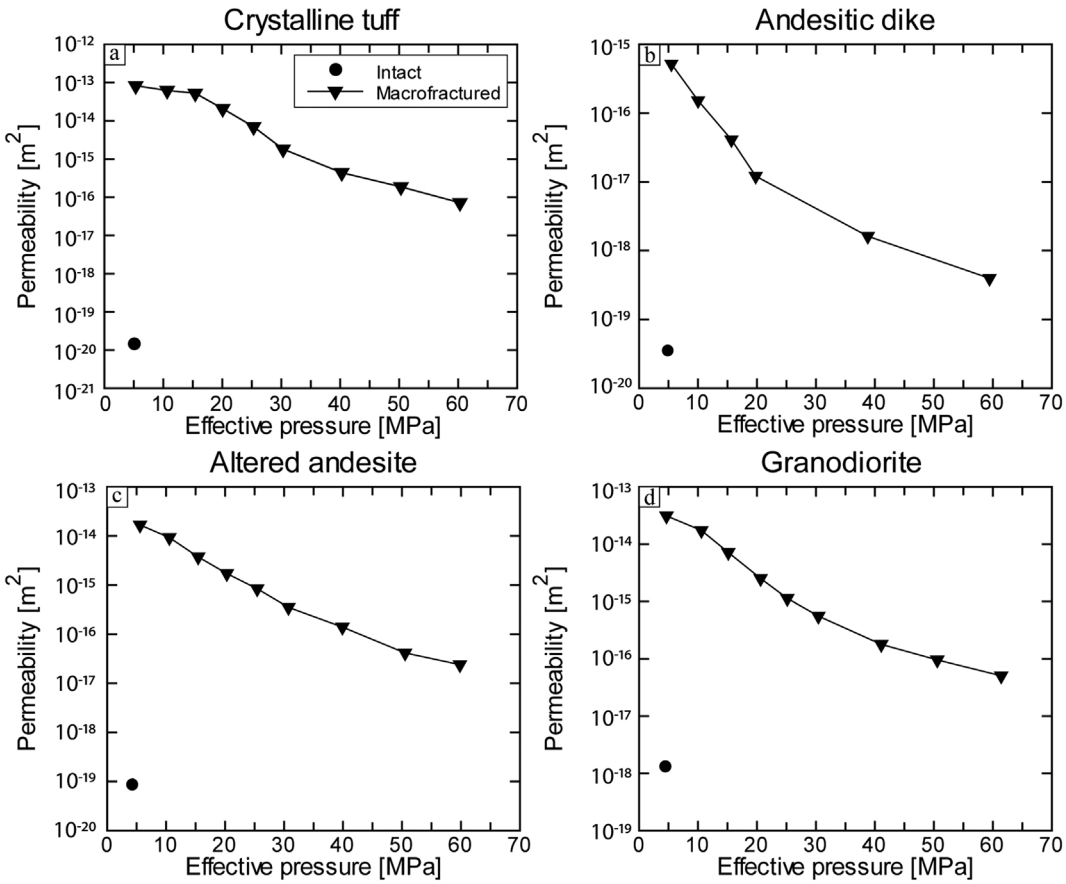

Fig. 8. Permeability of intact samples of (a) crystalline tuff, (b) andesitic dike, (c) altered andesite and (d) granodiorite at an effective pressure of 5 MPa, and of macro-fractured but mated samples of the same four rocks as a function of increasing effective pressure up to 60 MPa.

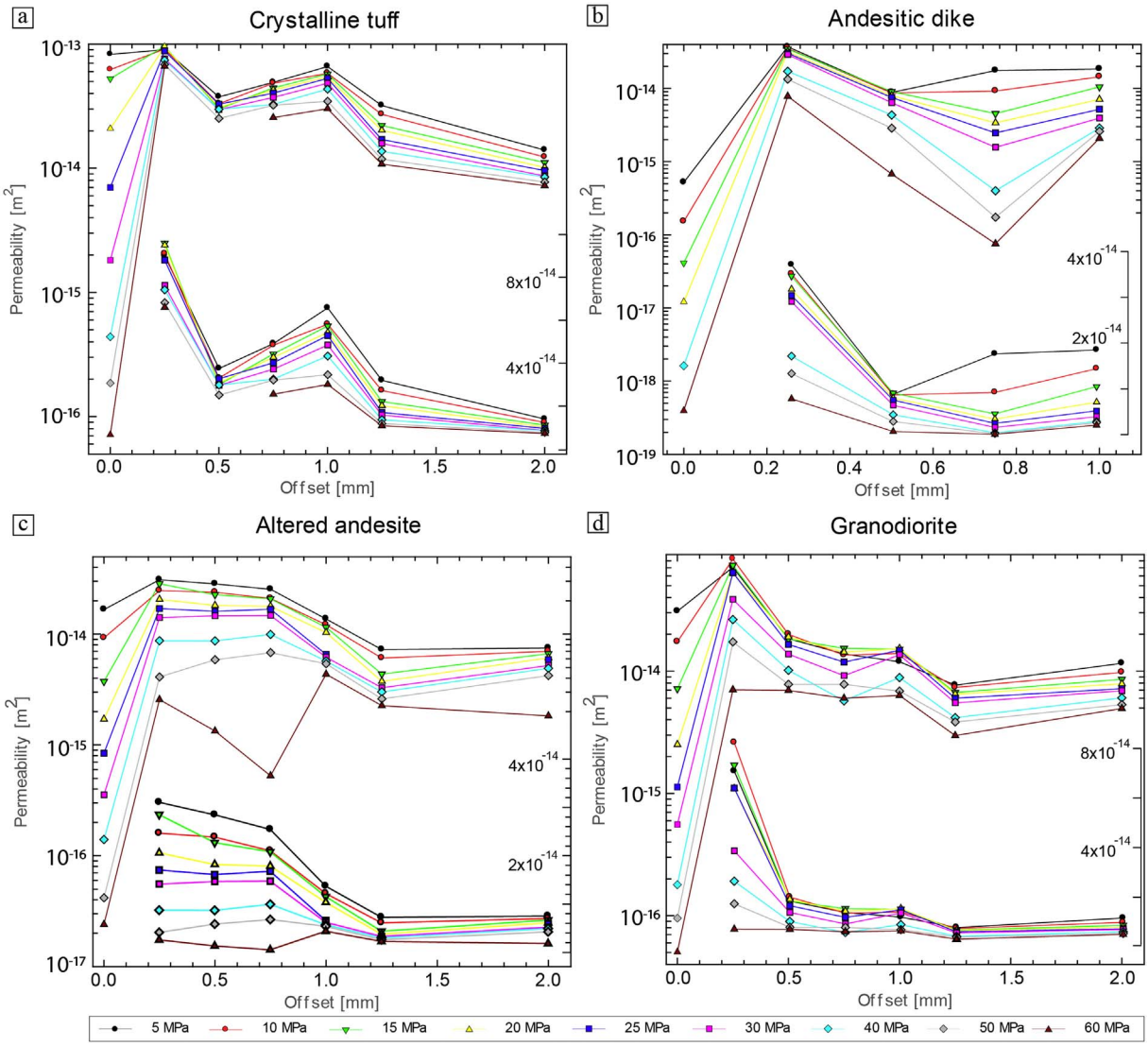

Fig. 9. Change in permeability of SVZ rocks samples as functions of increasing fracture offset and increasing effective pressure: (a) crystalline tuff, (b) andesite dike, (c) altered andesite and (d) granodiorite. Main figures show the data plotted on a logarithmic scale (left axis) and insets show the same data plotted on a linear scale (right axis).

decreasing as offset is increased. However, the fluctuation in permeability as a function of offset is variable and appears to depend on lithology. Both the crystalline tuff (Fig. 9a) and the andesite dike (Fig. 9b) record two permeability peaks, at offsets of 0.25 and 1.0 mm. By contrast, permeability in the altered andesite and granodiorite generally decreases with offset after the initial peak at 0.25 mm (Fig. 9c and d). Overall there does not appear to be any systematic variation of permeability with increasing offset.

4.3. Permeability of macro-fractured Seljadalur basalt as a function of fracture offset and gouge

For comparison, the permeability of macro-fractured samples of Seljadalur basalt are shown as functions of offset and effective pressure in Fig. 10, again plotted on both logarithmic and linear scales. Here, the permeability increases dramatically between zero offset (mated fracture) and the first offset of 0.25 mm, by between two and three orders of magnitude. However, in contrast to all the SVZ rocks, the permeability also continues to increase somewhat with increasing offset up to a value of around 1.5 mm, but at a decreasing rate. The permeability then decreases at higher offset values. As for the SVZ rocks, the permeability decreases with the increasing effective pressure for all values of offset. However, the decrease with increasing effective pressure is not uniform, with the pressure dependence exhibiting a remarkable peak at an offset of 1.5 mm where the permeability is also the highest. The pressure dependence then virtually disappears for effective pressure higher than about 40 MPa.

As noted earlier, we also made measurements of the permeability of macro-fractured samples of SB with an infilling layer of gouge. The methodology used for producing the gouge and filling the macro-fractures was identical to that reported in Wang et al. (2016). The results are shown in Fig. 11 as a function of both offset and gouge layer thickness. We observe that the sample with the mated (zero offset) macro-fracture has the highest permeability at low effective pressure, but there is a crossover region and the same sample has the lowest permeability at high effective pressure (Fig. 11a). This is consistent with the observations reported by Wang et al. (2016), and appears to occur because the gouge particles prop open the mated macro-fracture which would otherwise close up at elevated effective pressure and thus reduce the permeability significantly (as seen in the 'no gouge' curve of Fig. 11a). We also note that the permeability crossover pressure decreases substantially with increasing gouge layer thickness; with the crossover pressure being about 35 MPa for a gouge layer thickness of 0.3 mm and about 15 MPa for a gouge layer thickness of 1.0 mm.

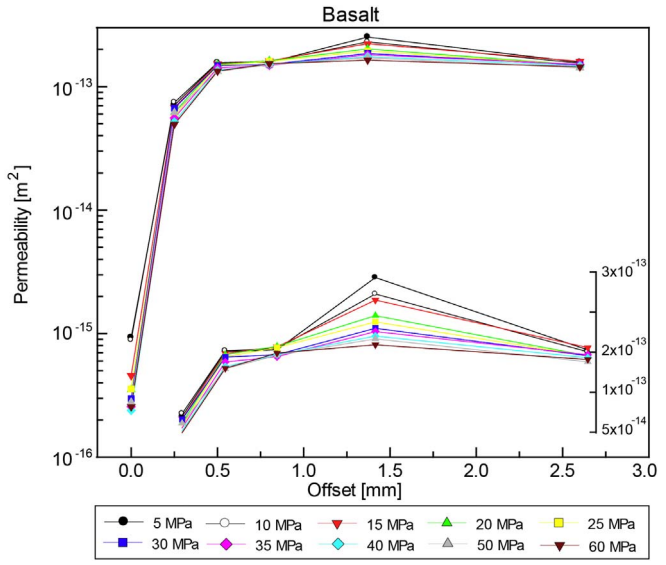

Fig. 10. Changes in permeability of Seljadalur basalt as a function of increasing fracture offset and increasing effective pressure. Main figure shows the data plotted on a logarithmic scale (left axis) and inset shows the same data plotted on a linear scale (right axis).

By contrast, the presence of a gouge layer within unmated macro-fractures decreases permeability for all values of layer thickness, as illustrated in Fig. 11b and c. This is entirely as expected, because the main effect of a gouge layer within the unmated fractures is to fill the aperture space created by the displacement of the rough fracture surfaces. In this way, the presence of a gouge layer appears to be able to counteract the effect of fracture offset, generally increasing permeability. But, the effect of the gouge layer on permeability is potentially complicated by the way in which it fills the aperture space. For example, the data of Fig. 11b show that the permeability increases with increasing gouge layer thickness. That is to be expected, since a thicker layer will provide more pathways for fluid flow. However, the data of Fig. 11c show that, for a larger fracture offset of 2 mm, the thinnest (0.3 mm) gouge layer gives the highest permeability; while thicker layers follow the previous trend. This is potentially because the thinnest gouge layer does not fully fill the larger fracture aperture at this larger offset, and a fracture that is only partially filled will provide additional void space for fluid flow. This interpretation is supported by the data of Fig. 11d, which shows that the permeability in the fracture containing the 0.3 mm thick gouge layer increases for all offsets greater than 1.25 mm regardless of the effective pressure.

4.4. Fracture trace analysis

4.4.1. Fracture characterization

In order to characterize the macro-fractures in our samples, we cut the cores axially in an orientation perpendicular to the fracture plane, thus producing a cross-section parallel to the fluid flow direction. These fracture traces were then digitized using Adobe Illustrator®, at a resolution of 0.05 mm (Fig. 12). We quantified the traces by their roughness and their aperture. The power spectrum is a robust technique that is well-suited for characterizing fault and fracture roughness (Babadagli and Develi, 2003; Candela et al., 2012, 2009; Persson et al.,

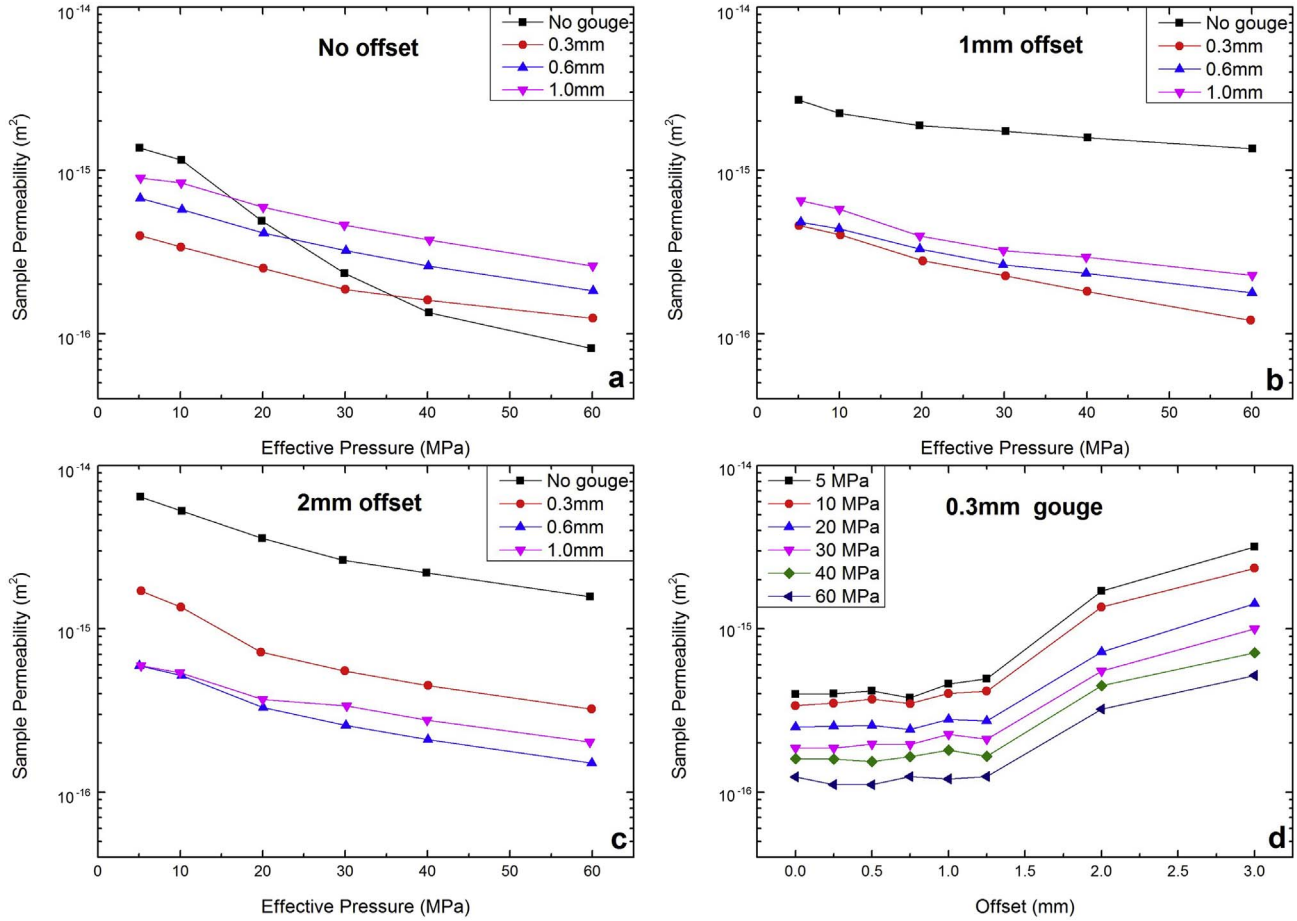

Fig. 11. Effect of the presence and thickness of a gouge layer on the permeability of mated (no offset) and un-mated (offsets from 0.25 to 3.0 mm) samples of SB as a function of increasing effective pressure.

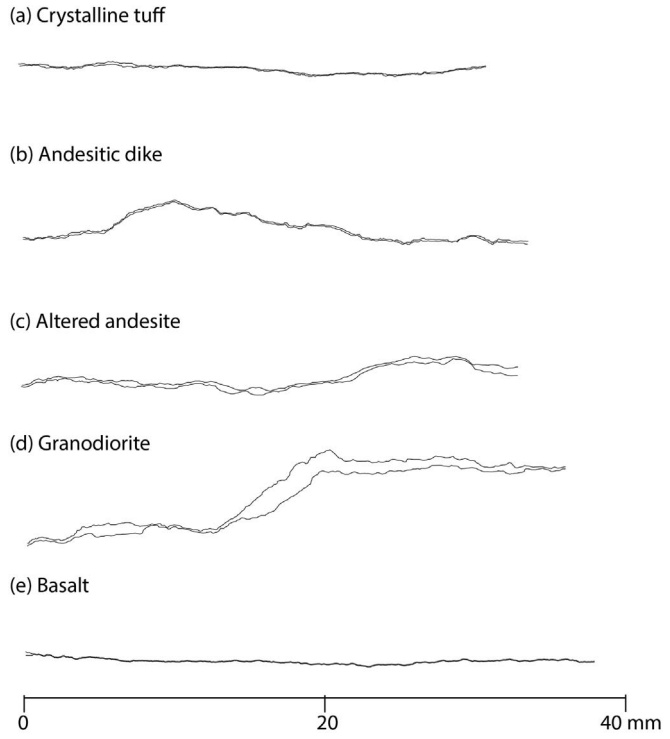

Fig. 12. Examples of fracture traces from sectioned rock samples to illustrate the fracture roughness parallel to the fluid flow direction. Horizontal and vertical axes are both at the same scale.

2005). We therefore calculate the power spectral density and spatial frequency from the fracture trace data using the Fast Fourier Transform (FFT) method (Cooley and Tukey, 1964) after correction for any linear alignment trend in the measured data (Fig. 13) (Kudo et al., 1992; Nara et al., 2006). From log-log plots of the power spectral density ($P(k) = Ck^{-1-2H}$) against the spatial frequency (reciprocal wavelength), we characterize the roughness by the slope (-1-2H), the Hurst, or roughness, exponent (H) and its pre-factor (C). The slope describes how the roughness varies with the scale, while the pre-factor describes the steepness of the surface or the total profile variance, which is a quantitative measure of the amplitude at a specified wavelength (Candela et al., 2012, 2011; Mandelbrot, 1983; Power and Tullis, 1991; Turcotte, 1992). The mean roughness exponents (H) and pre-factors, (C) for each lithology are given in Table 2. Thus, from the pre-factor values, the fractures with higher amplitudes are those of andesitic dike and altered andesite, while the lower amplitudes are those of crystalline tuff and basalt (Fig. 13 and Table 2). The slope and H show that the roughness is dominated by high frequencies (shortest wavelength).

The fracture aperture is defined as the separation between two opposing fracture surfaces (a_x), measured perpendicular to those surfaces (Lanaro, 2000). For each fracture trace (Fig. 12) we determined the mean aperture ($\overline{a}$) for each increment of offset, L_{off}, from the digitized traces after separating them by the minimum amount required to remove any overlap (Fig. 14). In Fig. 15, we show the relation between

Table 1
Table of sample material properties.

Rock	Composition	Grain size (mm)
Crystalline tuff	45%Pl–25%Lithic fragments-10%Px – 10%Glass-10%Bt	< 1
Andesitic dike	90%Pl-8%Hbl-2%Px	< 1–3 phenocrysts
Altered andesite	85%Pl-10%Hbl-5%Px	< 1–4 phenocrysts
Granodiorite	61%Pl-20%Qz-9%Kfs-8%Hbl-2%Bt	3–6
Seljadalur basalt	50%Pl-45%Px	< 1

Abbreviations: Bt = biotite, Hbl = hornblende, Kfs = K-feldspar, Pl = plagioclase, Px = pyroxene, Qz = Quartz (Whitney and Evans, 2010).

Table 2
Properties of the fracture traces for each lithology, showing the mean pre-factor, $\overline{C}$, the mean roughness exponent, $\overline{H}$, and their errors.

Lithology	$\overline{C}$	Error (±)	$\overline{H}$	Error (±)
Crystalline tuff	0.002	3.0×10^{-6}	0.665	0.021
Granodiorite	0.005	1.8×10^{-5}	0.523	0.014
Andesitic dike	0.007	3.7×10^{-5}	0.427	0.005
Altered Andesite	0.008	1.3×10^{-4}	0.597	0.111
Basalt	0.001	4.5×10^{-8}	0.487	0.002

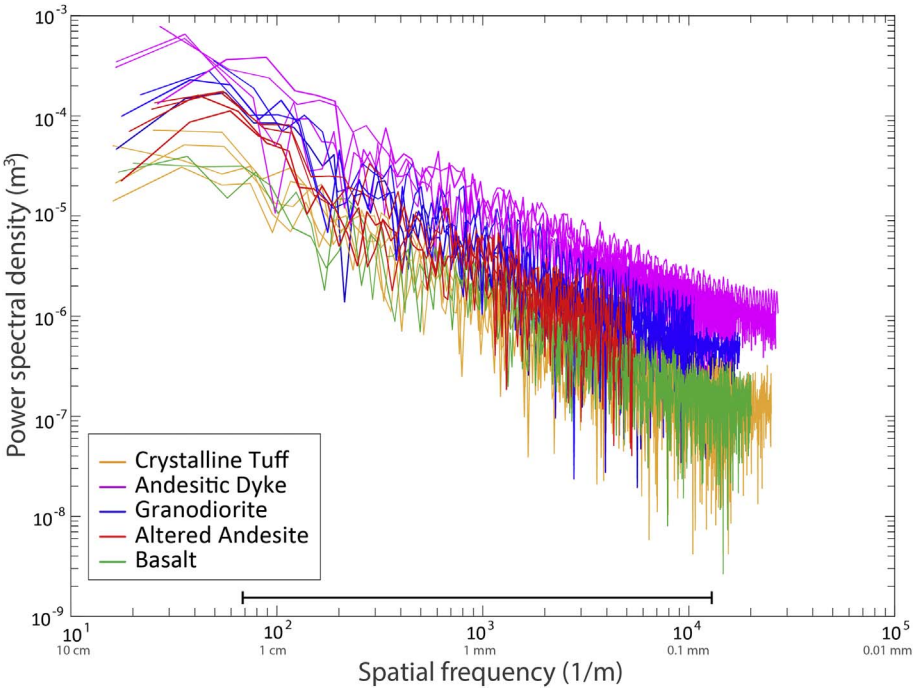

Fig. 13. Fourier power spectral density $P(k)$ as a function of the spatial frequency for fracture traces of each lithology.

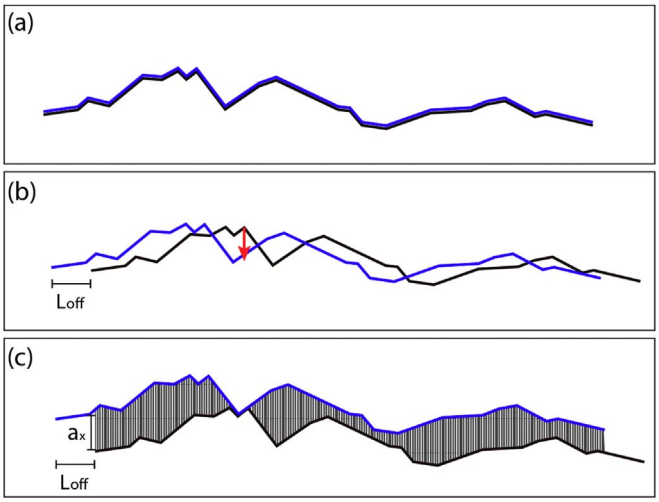

Fig. 14. Schematic diagram to illustrate the fracture aperture calculation method: (a) Mated fracture traces, (b) opposing traces displaced by the offset distance, L_{off}, (c) displaced traces separated by the minimum distance required to remove any overlap (red arrow). The mean aperture (ā) is then the arithmetic mean of all a_x. (For interpretation of the references to colour in this figure legend, the reader is referred to the web version of this article.)

aperture and offset length (L_{off}) determined from the digitized fracture traces of each lithology. For all lithologies, the primary trend is for apertures to increase dramatically with increasing offset up to some characteristic value in the range 0.5–1.0 mm. Apertures then increase only marginally with greater offset, but exhibit small oscillations with increasing offset for some lithologies (Fig. 15). We interpret these oscillations as simply a second order trend arising from local interactions between peaks and troughs on the opposing rough fracture surfaces.

5. Discussion

Our results show that the intact granodiorite sample has a permeability of 10^{-18} m^2, which is about two orders of magnitude higher than both the SVZ volcanic rocks (10^{-20} m^2) (Fig. 9) and the basalt (Nara et al., 2011). As a first-order approximation, this could favour the existence of geothermal reservoirs in intrusive rocks, which is the main lithology making up the SVZ basement south of 39°S. The permeability of all rocks increases significantly in samples containing mated macro-fractures (Fig. 8), similar to results reported by Nara et al. (2011). The permeability of samples with unmated macro-fractures increases even further, with respect to samples with mated macro-fractures, for all lithologies when the offset-length (L_{off}) is first increased (Fig. 9). At low effective pressure (P_{eff} = 5 MPa), this increase due to initial offset is around 2 orders of magnitude for the fresh volcanic rocks (andesitic dike and basalt) (Figs. 9 and 10) but less than one order of magnitude for the other rocks (Fig. 9). For all rocks, the permeability continues to increase with increasing offset until some characteristic value of L_{off} is reached; but the value is different for each different lithology. For higher values of offset, the permeability appears to change little, similar to the results obtained from shearing experiment reported by Esaki et al. (1999). However, we do observe some oscillation in the permeability values for given lithologies at higher offsets, and this may be a function of asperity contact, which will be different for each different lithology (e.g. Lanaro, 2000; Olsson and Barton, 2001). We observe a similar feature, as a function of increasing offset, in our fracture aperture analysis (Fig. 15).

A model that is widely applied in hydrogeology and related fields to relate fluid flow to fracture aperture is the *cubic law*, in which permeability is considered to be proportional to the cube of the mean aperture ($\bar{a}^3$) (e.g. Gudmundsson et al., 2012; Raven and Gale, 1985; Witherspoon et al., 1980; Zimmerman, 2012). The relation between permeability and mean aperture cubed, with increasing offset, is shown in Fig. 16. The general trends of the two sets of curves are similar, with both exhibiting a rapid initial increase with increasing offset. They then level off and exhibit little change with increasing offset above some characteristic offset value. However, the cubic law does not fully capture the very rapid transition from increasing values to steady values seen in the measured permeability data. Since the cubic law was derived for fluid flow between parallel plates, it is perhaps not surprising that it fails to capture all the details of fluid flow between two rough fracture surfaces. Furthermore, the aperture data in Fig. 16 were derived from single linear traces taken across the full fracture surface. This necessarily involves a loss of one dimension, and therefore likely also a loss of complexity. Nevertheless, the general trends are consistent.

The roughness index $\overline{H}$, derived from analysis of the fractures traces of Fig. 12 (Table 2), are shown in Fig. 17, plotted against the permeability of mated fractures (Fig. 17a) and against the difference in permeability between mated and un-mated fractures (Fig. 17b). For mated fractures, we see a general increase in permeability with increasing fracture roughness across all lithologies tested. In contrast, Fig. 17b shows that the increase in permeability for a fixed offset of 0.25 mm is highest for the lithologies with the lowest fracture roughnesses (andesite dike, basalt, and granodiorite) and lowest for those with the highest fracture roughnesses (crystalline tuff and altered andesite). The variation in roughness is relatively well constrained for most of the lithologies tested, except for the altered andesite where the range is very wide. This may be due to the alteration and mineralogical changes that have occurred in this material.

The characteristic value of offset coincides with minimum contact area between fracture surfaces, which also corresponds to the point where the mean aperture reaches a plateau value and hence the capacity for the fluid flow is also maximized (Min et al., 2004; Watanabe et al., 2008). Furthermore, since this is the minimum contact area, it is the point where the permeability is most pressure sensitive. The characteristic value of offset will therefore depend on the scale or the wavelength of fracture roughness, and hence on the aperture distribution. Although the permeability of un-mated fractures decreases with increasing P_{eff} for each increment of offset, it never drops below the permeability of samples with mated macro-fractures. Hence, permeability will always be dominated by un-mated fractures.

Since each sample was subjected to multiple pressurization cycles over a range of offsets, it was felt necessary to ascertain whether our experimental procedure could have induced additional damage during experiments. Therefore, after pressurization and measurement at the maximum offset, we re-ground the basalt sample to remove the total offset so that we could re-mate the fractures and then re-measure the mated fracture permeability. The results are presented in Fig. 18 and show that the permeabilities of the re-mated fracture returns to values of the same order as the initial mated values. However, the permeability range is somewhat higher for the re-mated fracture, which indicates a higher pressure sensitivity. This suggests that our experimental procedure causes only minimal additional damage, which was not great enough to significantly affect our overall results.

Our results show the changes in permeability that result from discrete fracture offsets. In nature, this corresponds to conditions where pore fluid pressure is higher than the least principal stress and fractures are able to become offset with minimal contact (e.g. hydrofractures), and therefore with minimum generation of wear products (e.g. fault gouge or cataclastic material). Our study does not consider the condition where fractures are subjected to shear displacement under higher normal stress producing wear products that may partially fill fracture apertures.

Many field and laboratory studies demonstrate that fracture damage zones exhibit the highest permeabilities within the overall fault structure (e.g. Brogi, 2008; Brogi et al., 2011; Caine et al., 1996; Caine and Forster, 1999; Evans et al., 1997; Liotta et al., 2010; Mitchell and

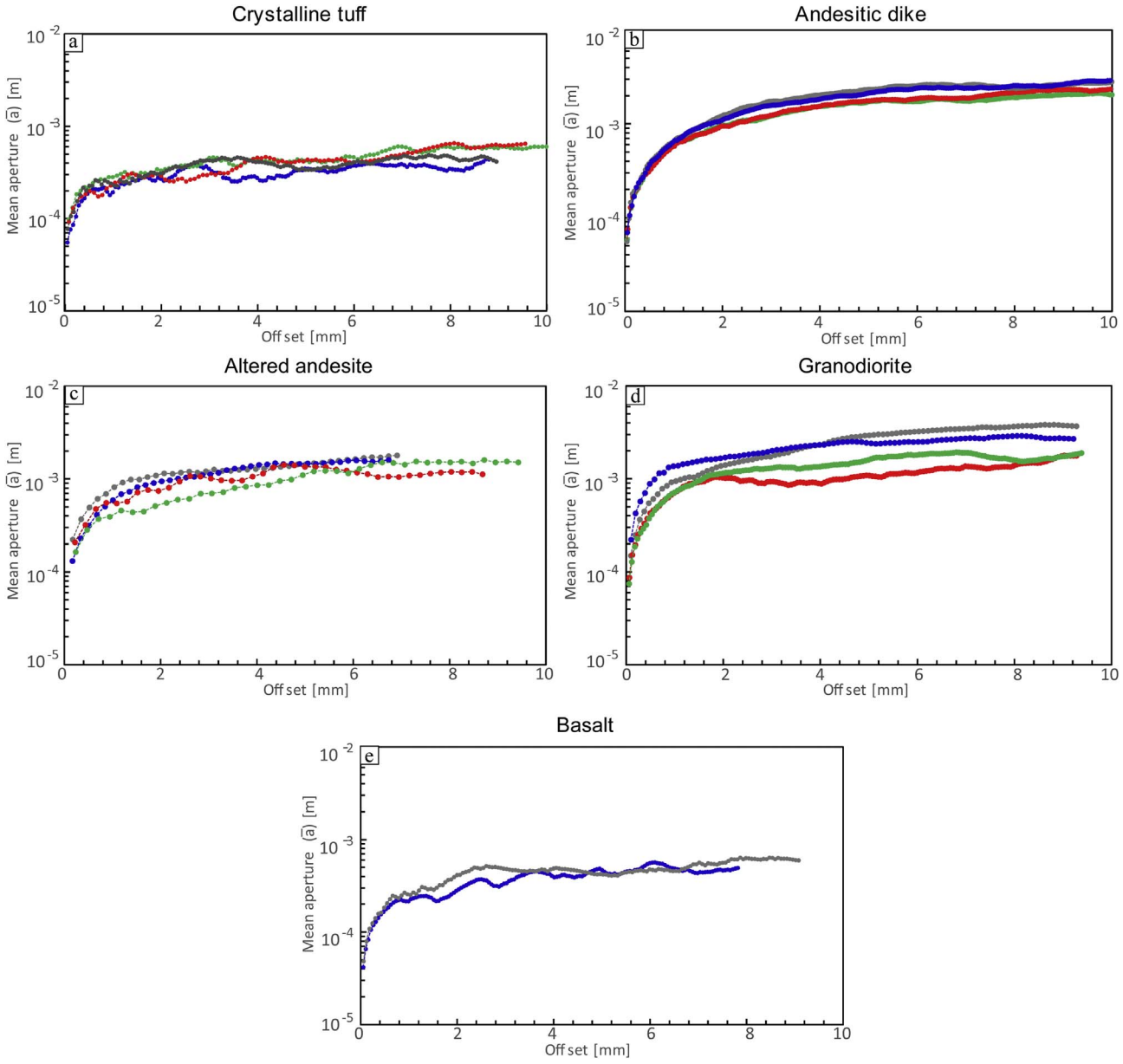

Fig. 15. Change in mean aperture (ā) as a function of increasing fracture offset; calculated for several fracture traces (denoted by different colors) of each lithology: (a) crystalline tuff, (b) andesite dike, (c) altered andesite (d) granodiorite and (e) basalt, using the methodology described in the text. (For interpretation of the references to colour in this figure legend, the reader is referred to the web version of this article.)

Faulkner, 2012; Walker et al., 2013). Our results indicate that while mated macro-fractures can maintain high permeability conditions ($k \approx 10^{-16}$ m^2) up to $P_{eff} \approx 40$ MPa (Fig. 2), such conditions can only be reached for un-mated fractures (i.e. those with a finite offset) at higher effective pressures.

In Fig. 19 we compare our measurements on the basement rocks of the SVZ with the range of intrinsic permeability for consolidated rocks (Brace, 1980), the permeability of clay-rich fault gouge from large-displacement fault zones (Faulkner and Rutter, 2000; Wibberley and Shimamoto, 2003), estimates of seismogenic permeability (SP) from migration of microearthquakes (Talwani and Acree, 1985) and the bulk permeability of the Ohaaki-Broadlands & Wairakei geothermal systems in New Zealand (Rowland and Sibson, 2004). All these data are presented in the context of the critical bounds of permeability that allow either hydrothermal convection (Cathles et al., 1997) or the development of forced overpressures (Neuzil, 1995). Importantly, we find that all the measurements for intact samples lie within the forced overpressure regime, whereas all those for offset macrofractures lie within the hydrothermal flow regime where advective/convective flow occurs. We also find that the measurements for mated macrofractures span the two regimes. Hence, as the permeability of all the lithologies with offset macrofractures is higher than 10^{-16} m^2 over the entire range of effective pressures measured, this suggests that the development of hydrothermal convection cells is favoured in basement rocks containing fracture systems with finite offset. This is particularly apparent in the granodiorite and crystalline tuff which record high values of permeability, even at high effective pressures.

This observation implies that significant permeability can be maintained in NE-striking fault systems of the SVZ, which have an extensional component, and in WNW-striking fault zones under overpressured fluid conditions, as described by Pérez-Flores et al. (2016). Any fracture filling and sealing would tend to obstruct fluid flow through the fracture networks, but any reactivation of the faults would tend to enhance it. Such small-scale fault reactivation could also be

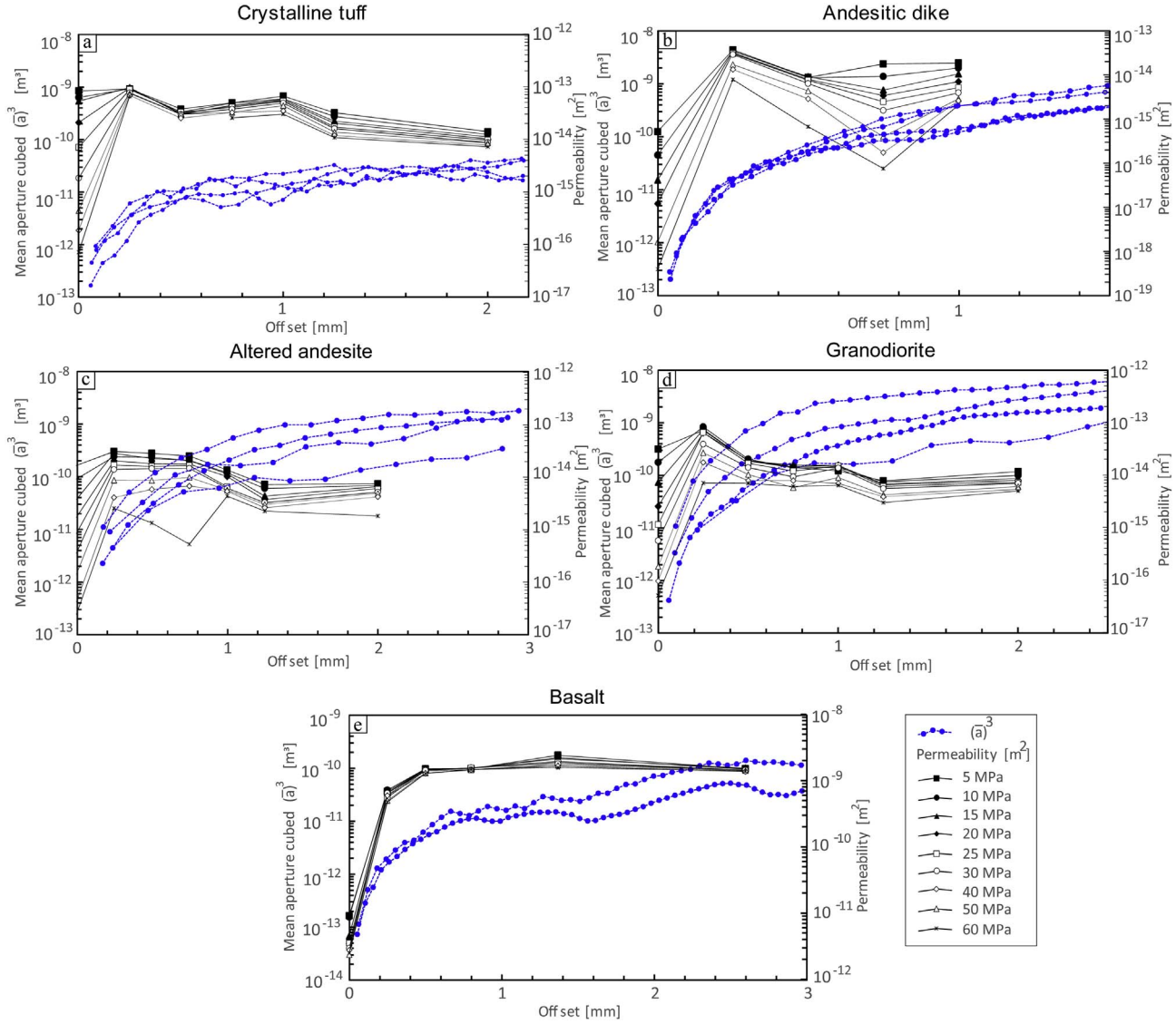

Fig. 16. Composite plots showing, for each lithology, a comparison between the permeability of unmated macro-fractured samples (gray lines)and the cube of the calculated mean fracture aperture for several fracture traces (blue dots) of each lithology: (a) crystalline tuff, (b) andesite dike, (c) altered andesite (d) granodiorite and (e) basalt, as functions of increasing offset and effective pressure. (For interpretation of the references to colour in this figure legend, the reader is referred to the web version of this article.)

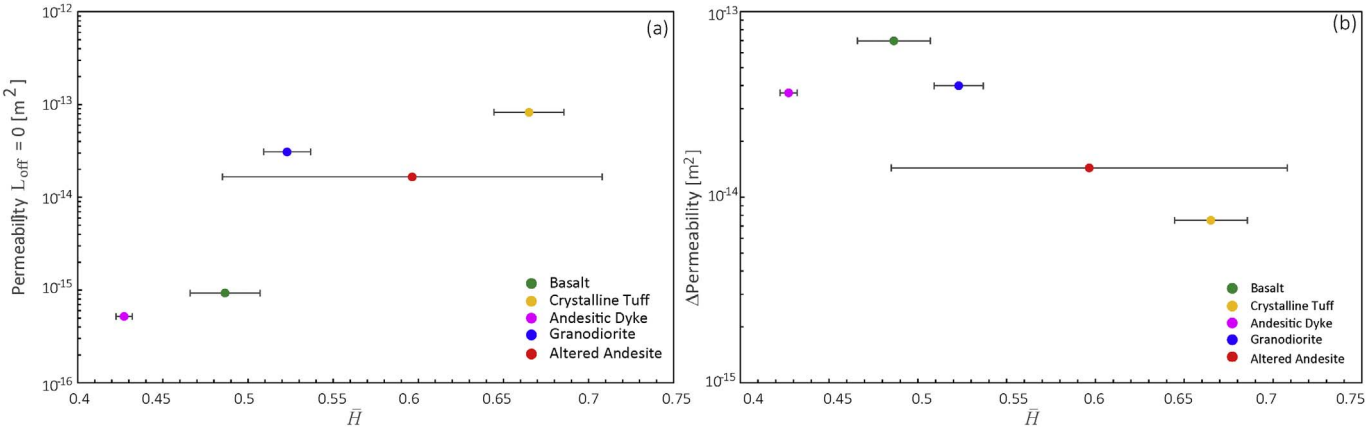

Fig. 17. (a) Comparison of the permeability of samples with mated macro-fractures and the mean roughness index $\bar{H}$ for each lithology under an effective pressure of 5 MPa; (b) The incremental change in permeability between samples with mated macro-fractures (L_{off} = 0) and those with unmated macro-fractures and an offset (L_{off}) of 0.25 mm, as a function of the mean roughness index $\bar{H}$ for each lithology. The error bars indicate the standard deviation of the mean roughness.

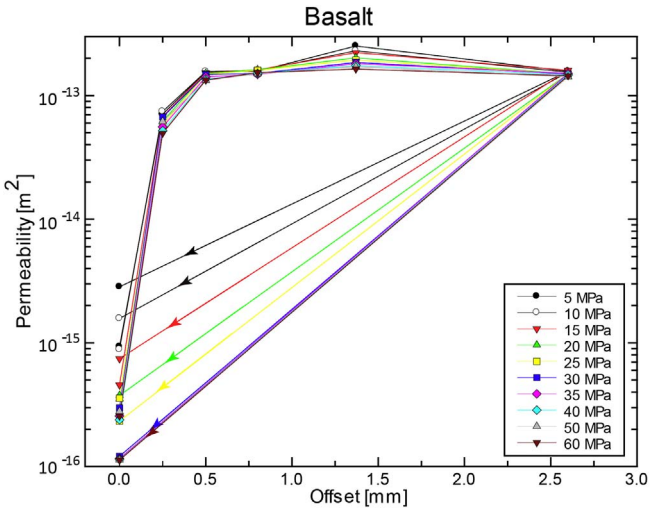

Fig. 18. Permeability measurements with increasing offset and increasing effective pressure for Seljadalur basalt, together with final measurements made on the re-ground and re-mated sample. The permeabilities of the re-mated sample return to values within the same order as the initial mated values, indicating that the experimental process caused very little, if any, additional damage.

enhanced by moderate interseismic fault slip rates, such as those of 7.0 and 0.5 mm/yr for the LOFS and ATF, respectively, as reported by Stanton-Yonge et al. (2016).

Independent evidence of the potential for fractured plutonic rocks to provide fluid conduits along fault damage zones and hence act as fluid reservoirs is provided in the magnetotelluric (MT) study by Held et al. (2016). Their measurements indicate domains of high fluid conductivity along NNE-striking master faults of the LOFS and WNW-striking faults of the ATF in the vicinity and north of Villarrica volcano (SVZ, Fig. 1). Held et al. (2016) also show a high conductivity anomaly in the lower crust apparently connected to the LOFS and ATF. Furthermore, the intact low permeability lithologies or alteration zones may act as cap rocks, and this is likely to increase the time span and integrity of reservoir conditions, as has been modelled by Sanchez-Alfaro et al. (2016) for the Tolhuaca volcano (Fig. 1b). Their research shows a low permeability zone, with similar permeability values to those of our intact volcanic rocks ($< 10^{-18}$ m^2), which acts as a cap rock. Finally, our results suggest that the architecture of a geothermal system within the SVZ might involve a combination of high-permeability, fractured plutonic-volcanic rocks as the reservoir, together with low-permeability, intact volcanic rock strata, enhanced by argillaceous alteration, as the cap-rock (Sanchez-Alfaro et al., 2016).

6. Conclusions

We report results from the first permeability measurements made on intact and fractured samples of basement rocks from the Southern Andes Volcanic Zone. These provide us with a quantitative overview of the variation of permeability within fault zones under increasing effective pressure that mimics their behaviour at depth.

1. Of the four SVZ rock types tested, the granodiorite and the crystalline tuff exhibit the highest and lowest intact rock permeabilities, respectively.
2. The introduction of mated macro-fractures increases permeability by around 4 orders of magnitude in the granodiorite and 7 orders of magnitude in the crystalline tuff at low effective pressure.
3. Offsetting the mated macro-fractures to produce unmated macro-fractures increases the permeability further by up to several orders of magnitude, depending on the lithology, the effective pressure and the offset length.
4. For all rocks, permeability increases with increasing offset up to some characteristic value, after which it changes little but exhibits oscillatory behaviour. The characteristic offset value is different for each lithology and appears to depend on fracture roughness.
5. In all cases, increasing the effective pressure decreases both the permeability and its oscillatory behaviour. However, offset (unmated) macro-fractures play a key role in maintaining fracture permeability even under the highest effective pressure tested (60 MPa).

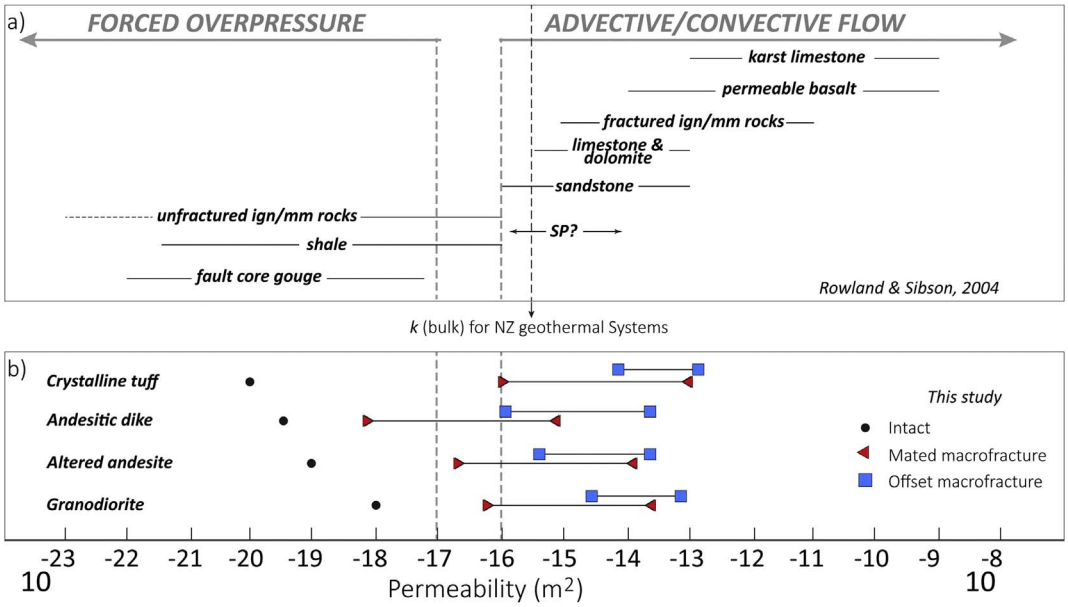

Fig. 19. a) The range of intrinsic permeability for consolidated rocks (Brace, 1980) in comparison to that of clay-rich fault gouge from large-displacement fault zones (Faulkner and Rutter, 2000; Wibberley and Shimamoto, 2003), and estimates of seismogenic permeability (SP) from migration of microearthquakes (Talwani and Acree, 1985). Also shown are the critical bounds of permeability that allow either hydrothermal convection (Cathles et al., 1997) or the development of forced overpressures (Neuzil, 1995), and the bulk permeability for several large geothermal fields in New Zealand (NZ). Modified from Rowland and Sibson (2004). b) The range of permeabilities for the four SVZ lithologies tested in this study for intact, mated macrofracture and offset macrofracture configurations. All the measurements for intact samples lie within the forced overpressure regime, whereas all those for offset macrofractures lie within the hydrothermal flow regime. The measurements for mated macrofractures span between the two regimes.

6. Filling offset fractures with gouge decreases their permeability and virtually eliminates the oscillatory behaviour.
7. For all four SVZ lithologies, the permeability of intact samples lie within the forced overpressure regime, whereas all those for offset macrofractures lie within the hydrothermal flow regime where advective/convective flow occurs.
8. Since the higher permeability granodioritic plutonic rocks dominate the SVZ basement they may, when containing offset fractures, be able both to provide permeable pathways for fluid flow along faults and also provide enough fluid storage to constitute a viable geothermal reservoir.

Acknowledgements

We are grateful to John Bowles, Steve Boon, and Neil Hughes for their essential support during laboratory experiments. Special thanks to Jim Davy for generous help during rock sample preparation. PPF thanks the UCL Earth Science community, and especially the Seismolab group, for their collaboration and friendship during her internship at UCL. We sincerely thank Editor Toru Takeshita and reviewers Philip Benson and Andrea Brogi; they provided very useful comments and criticism that helped to improve the manuscript. Thanks to Gonzalo Yáñez for his continuous advise and help. Thanks to Pablo Iturrieta for his programming help and to Felipe Aron, Rodrigo Gomila and Gerd Sielfeld for their fruitful discussions and ideas. This work was partly funded by NERC award NE/N002938/1. This paper is a contribution to the Andean Geothermal Center of Excellence (CEGA) FONDAP/CONICYT Projects 15090013 and 1141139 (JC). PPF's PhD studies are funded by CONICYT-Beca Doctorado Nacional 21120519.

References

Angermann, D., Klotz, J., Reigber, C., 1999. Space-geodetic estimation of the Nazca-South America Euler vector. Earth Planet. Sci. Lett. 171, 329–334. http://dx.doi.org/10.1016/S0012-821X(99)00173-9.

Arancibia, G., Cembrano, J., Lavenu, A., 1999. Transpresión dextral y partición de la deformación en la Zona de Falla Liquiñe-Ofqui, Aisén, Chile (44–45°S). Rev. Geol. Chile 26. http://dx.doi.org/10.4067/S0716-02081999000100001.

Aravena, D., Muñoz, M., Morata, D., Lahsen, A., Parada, M.Ángel, Dobson, P., 2016. Assessment of high enthalpy geothermal resources and promising areas of Chile. Geothermics 59. http://dx.doi.org/10.1016/j.geothermics.2015.09.001.

Babadagli, T., Develi, K., 2003. Fractal characteristics of rocks fractured under tension. Theor. Appl. Fract. Mech. 39, 73–88. http://dx.doi.org/10.1016/S0167-8442(02)00139-8.

Barrientos, S.E., Acevedo-Aránguiz, P.S., 1992. Seismological aspects of the 1988–1989 Lonquimay (Chile) volcanic eruption. J. Volcanol. Geotherm. Res. 53, 73–87. http://dx.doi.org/10.1016/0377-0273(92)90075-O.

Barton, C. a, Zoback, M.D., Moos, D., 1995. Fluid fow along potentially active faults in crystalline rock. Geology 23, 683–686. http://dx.doi.org/10.1130/0091-7613(1995)023<0683:Ffapaf>2.3.Co;2.

Benson, P.M., Meredith, P.G., Schubnel, A., 2006a. Role of void space geometry in permeability evolution in crustal rocks at elevated pressure. J. Geophys. Res. Solid Earth 111, 1–14. http://dx.doi.org/10.1029/2006JB004309.

Benson, P.M., Schubnel, A., Vinciguerra, S., Trovato, C., Meredith, P., Young, R.P., 2006b. Modeling the permeability evolution of microcracked rocks from elastic wave velocity inversion at elevated isostatic pressure. J. Geophys. Res. Solid Earth 111, 1–11. http://dx.doi.org/10.1029/2005JB003710.

Bistacchi, A., Ashley Griffith, W., Smith, S.A.F., di Toro, G., Jones, R., Nielsen, S., 2011. Fault roughness at seismogenic depths from LIDAR and photogrammetric analysis. Pure Appl. Geophys. 168, 2345–2363. http://dx.doi.org/10.1007/s00024-011-0301-7.

Brace, W.F., 1980. Permeability of crystalline and argillaceous rocks. Int. J. Rock Mech. Min. Sci. Geomech. Abstr. 17.

Brogi, A., 2008. Fault zone architecture and permeability features in siliceous sedimentary rocks: insights from the Rapolano geothermal area (Northern Apennines, Italy). J. Struct. Geol. 30, 237–256. http://dx.doi.org/10.1016/j.jsg.2007.10.004.

Brogi, A., Fabbrini, L., Liotta, D., 2011. Sb-Hg ore deposit distribution controlled by brittle structures: the case of the Selvena mining district (Monte Amiata, Tuscany, Italy). Ore Geol. Rev. 41, 35–48. http://dx.doi.org/10.1016/j.oregeorev.2011.06.004.

Brogi, A., Novellino, R., 2015. Low angle normal fault (LANF)-zone architecture and permeability features in bedded carbonate from inner northern Apennines (Rapolano Terme, Central Italy). Tectonophysics 638, 126–146. http://dx.doi.org/10.1016/j.tecto.2014.11.005.

Caine, J.S., Bruhn, R.L., Forster, C.B., 2010. Internal structure, fault rocks, and inferences regarding deformation, fluid flow, and mineralization in the seismogenic Stillwater normal fault, Dixie Valley, Nevada. J. Struct. Geol. 32, 1576–1589. http://dx.doi.org/10.1016/j.jsg.2010.03.004.

Caine, J.S., Evans, J.P., Forster, C.B., 1996. Fault zone architecture and permeability structure. Geology. http://dx.doi.org/10.1130/0091-7613(1996)024<1025.

Caine, J.S., Forster, C.B., 1999. Fault Zone Architecture and Fluid Flow: Insights from Field Data and Numerical Modeling.

Candela, T., Renard, F., Bouchon, M., Brouste, A., Marsan, D., Schmittbuhl, J., Voisin, C., 2009. Characterization of fault roughness at various scales: implications of three-dimensional high resolution topography measurements. Pure Appl. Geophys. 166, 1817–1851. http://dx.doi.org/10.1007/s00024-009-0521-2.

Candela, T., Renard, F., Klinger, Y., Mair, K., Schmittbuhl, J., Brodsky, E.E., 2012. Roughness of fault surfaces over nine decades of length scales. J. Geophys. Res. Solid Earth 117, 1–30. http://dx.doi.org/10.1029/2011JB009041.

Candela, T., Schmittbuhl, J., Bouchon, M., Brodsky, E.E., 2011. Fault Slip Distribution and Fault Roughness. pp. 959–968. http://dx.doi.org/10.1111/j.1365-246X.2011.05189.x.

Cathles, L.M., Erendi, A.H.J., Barrie, T., 1997. How long can a hydrothermal system Be sustained by single intrusive event? Econ. Geol. 92, 766–771.

Cembrano, J., Herve, F., Lavenu, A., 1996. The Liquifie Ofqui fault zone: a long-lived intra-arc fault system in southern Chile. Tectonophysics 256, 55–56.

Cembrano, J., Lara, L., 2009. The link between volcanism and tectonics in the southern volcanic zone of the Chilean Andes: a review. Tectonophysics 471, 96–113. http://dx.doi.org/10.1016/j.tecto.2009.02.038.

Cembrano, J., Schermer, E., Lavenu, A., Sanhueza, A., 2000. Contrasting nature of deformation along an intra-arc shear zone, the Liquiñe – Ofqui fault zone, southern Chilean Andes. Tectonophysics 319, 129–149. http://dx.doi.org/10.1016/S0040-1951(99)00321-2.

Cooley, J.W., Tukey, J.W., 1964. An algorithm for the machine calculation of complex fourier series. Math. Comput. 19, 297–301.

Cox, S.F., 2007. Structural and isotopic constraints on fluid flow regimes and fluid pathways during upper crustal deformation: an example from the Taemas area of the Lachlan Orogen, SE Australia. J. Geophys. Res. 112, 1–23. http://dx.doi.org/10.1029/2006JB004734.

Cox, S.F., 1999. Deformational controls on the dynamics of fluid flow in mesothermal gold systems. Geol. Soc. Lond. Spec. Publ. 155, 123–140. http://dx.doi.org/10.1144/GSL.SP.1999.155.01.10.

Curewitz, D., Karson, J. a, 1997. Structural settings of hydrothermal outflow: fracture permeability maintained by fault propagation and interaction. J. Volcanol. Geotherm. Res. 79, 149–168. http://dx.doi.org/10.1016/S0377-0273(97)00027-9.

Eccles, D., Sammonds, P.R., Clint, O.C., 2005. Laboratory studies of electrical potential during rock failure. Int. J. Rock Mech. Min. Sci. 42, 933–949. http://dx.doi.org/10.1016/j.ijrmms.2005.05.018.

Esaki, T., Du, S., Mitani, Y., Ikusada, K., Jing, L., 1999. Development of a shear-flow test apparatus and determination of coupled properties for a single rock joint. Int. J. Rock Mech. Min. Sci. 36, 641–650. http://dx.doi.org/10.1016/S0148-9062(99)00044-3.

Evans, J.P., Forster, C.B., Goddard, J.V., 1997. Permeability of fault-related rocks, and implications for hydraulic structure of fault zones. J. Struct. Geol. 19, 1393–1404. http://dx.doi.org/10.1016/S0191-8141(97)00057-6.

Faulkner, D.R., Armitage, P.J., 2013. The effect of tectonic environment on permeability development around faults and in the brittle crust. Earth Planet. Sci. Lett. 375, 71–77. http://dx.doi.org/10.1016/j.epsl.2013.05.006.

Faulkner, D.R., Jackson, C.A.L., Lunn, R.J., Schlische, R.W., Shipton, Z.K., Wibberley, C. a. J., Withjack, M.O., 2010. A review of recent developments concerning the structure, mechanics and fluid flow properties of fault zones. J. Struct. Geol. http://dx.doi.org/10.1016/j.jsg.2010.06.009. Elsevier Ltd.

Faulkner, D.R., Rutter, E.H., 2000. Comparisons of water and argon permeability in natural clay-bearing fault gouge under high pressure at 20°C. J. Geophys. Res. 105, 16415. http://dx.doi.org/10.1029/2000JB900134.

Faulkner, D.R., Rutter, E.H., 1998. The gas permeability of clay-bearing fault gouge at 20°C. Geol. Soc. Lond. Spec. Publ. 147, 147–156. http://dx.doi.org/10.1144/gsl.sp.1998.147.01.10.

Griffith, W.A., Nielsen, S., Di Toro, G., Smith, S.A.F., 2010. Rough faults, distributed weakening, and off-fault deformation. J. Geophys. Res. Solid Earth 115. http://dx.doi.org/10.1029/2009JB006925.

Gudmundsson, A., Kusumoto, S., Simmenes, T.H., Philipp, S.L., Larsen, B., Lotveit, I.F., 2012. Effects of overpressure variations on fracture apertures and fluid transport. Tectonophysics 581, 220–230. http://dx.doi.org/10.1016/j.tecto.2012.05.003.

Gudmundsson, A., Simmenes, T.H., Larsen, B., Philipp, S.L., 2010. Effects of internal structure and local stresses on fracture propagation, deflection, and arrest in fault zones. J. Struct. Geol. 32, 1643–1655. http://dx.doi.org/10.1016/j.jsg.2009.08.013.

Held, S., Schill, E., Pavez, M., Díaz, D., Muñoz, G., Morata, D., Kohl, T., 2016. Resistivity distribution from mid-crustal conductor to near-surface across the 1200 km long Liquiñe-Ofqui Fault System, southern Chile. Geophys. J. Int. 207, 1387–1400. http://dx.doi.org/10.1093/gji/ggw338.

Kim, Y.-S., Peacock, D.C., Sanderson, D.J., 2004. Fault damage zones. J. Struct. Geol. 26, 503–517. http://dx.doi.org/10.1016/j.jsg.2003.08.002.

Kudo, Y., Sano, O., Murashige, N., Mizuta, Y., Nakagawa, K., 1992. Stress-induced crack path in Aji granite under tensile stress. Pure Appl. Geophys. PAGEOPH 138, 641–656. http://dx.doi.org/10.1007/BF00876342.

Lahsen, A., Rojas, J., Morata, D., Aravena, D., 2015a. Geothermal exploration in Chile: country update. World Geotherm. Congr. 2015, 1–7.

Lahsen, A., Rojas, J., Morata, D., Aravena, D., 2015b. Exploration for High-temperature Geothermal Resources in the Andean Countries of South America. 1996. pp. 19–25.

Lamur, A., Kendrick, J.E., Eggertsson, G.H., Wall, R.J., Ashworth, J.D., Lavallée, Y., 2017. The permeability of fractured rocks in pressurised volcanic and geothermal systems. Sci. Rep. 7, 6173. http://dx.doi.org/10.1038/s41598-017-05460-4.

Lanaro, F., 2000. A random field model for surface roughness and aperture of rock fractures. Int. J. Rock Mech. Min. Sci. 37, 1195–1210. http://dx.doi.org/10.1016/S1365-1609(00)00052-6.

Lange, D., Cembrano, J., Rietbrock, A., Haberland, C., Dahm, T., Bataille, K., 2008. First seismic record for intra-arc strike-slip tectonics along the Liquiñe-Ofqui fault zone at the obliquely convergent plate margin of the southern Andes. Tectonophysics 455, 14–24. http://dx.doi.org/10.1016/j.tecto.2008.04.014.

Lara, L., Lavenu, A., Cembrano, J., Rodriguez, C., 2006. Structural controls of volcanism in transversal chains: resheared faults and neotectonics in the Cordón Caulle–Puyehue area (40.5°S), Southern Andes. J. Volcanol. Geotherm. Res. 158, 70–86. http://dx.doi.org/10.1016/j.jvolgeores.2006.04.017.

Lara, L.E., Cembrano, J., Lavenu, A., 2008. Quaternary vertical displacement along the Liquiñe-Ofqui Fault Zone: differential uplift and coeval volcanism in the southern Andes? Int. Geol. Rev. 50, 975–993. http://dx.doi.org/10.2747/0020-6814.50.11.975.

Lavenu, A., Cembrano, J., 1999. Compressional- and transpressional-stress pattern for Pliocene and Quaternary brittle deformation in fore arc and intra-arc zones (Andes of Central and Southern Chile). J. Struct. Geol. 21, 1669–1691. http://dx.doi.org/10.1016/S0191-8141(99)00111-X.

Legrand, D., Barrientos, S., Bataille, K., Cembrano, J., Pavez, a., 2011. The fluid-driven tectonic swarm of Aysen Fjord, Chile (2007) associated with two earthquakes (Mw = 6.1 and Mw = 6.2) within the Liquiñe-Ofqui Fault zone. Cont. Shelf Res. 31, 154–161. http://dx.doi.org/10.1016/j.csr.2010.05.008.

Liotta, D., Brogi, A., Meccheri, M., Dini, A., Bianco, C., Ruggieri, G., 2015. Coexistence of low-angle normal and high-angle strike- to oblique-slip faults during Late Miocene mineralization in eastern Elba Island (Italy). Tectonophysics 660, 17–34. http://dx.doi.org/10.1016/j.tecto.2015.06.025.

Liotta, D., Ruggieri, G., Brogi, A., Fulignati, P., Dini, A., Nardini, I., 2010. Migration of geothermal fluids in extensional terrains: the ore deposits of the Boccheggiano-Montieri area (southern Tuscany, Italy). Int. J. Earth Sci. 99, 623–644. http://dx.doi.org/10.1007/s00531-008-0411-3.

Mandelbrot, B.B., 1983. The fractal geometry of nature. Am. J. Phys. http://dx.doi.org/10.1017/CBO9781107415324.004. W. H. Freeman and Company, New York.

Meixner, J., Schill, E., Grimmer, J.C., Gaucher, E., Kohl, T., Klingler, P., 2016. Structural control of geothermal reservoirs in extensional tectonic settings: an example from the Upper Rhine Graben. J. Struct. Geol. 82, 1–15. http://dx.doi.org/10.1016/j.jsg.2015.11.003.

Melnick, D., Folguera, A., Ramos, V., 2006. Structural control on arc volcanism: the caviahue–copahue complex, central to patagonian Andes transition (38°S). J. South Am. Earth Sci. 22, 66–88. http://dx.doi.org/10.1016/j.jsames.2006.08.008.

Micklethwaite, S., Sheldon, H. a., Baker, T., 2010. Active fault and shear processes and their implications for mineral deposit formation and discovery. J. Struct. Geol. 32, 151–165. http://dx.doi.org/10.1016/j.jsg.2009.10.009.

Min, K.-B., Rutqvist, J., Tsang, C.-F., Jing, L., 2004. Stress-dependent permeability of fractured rock masses: a numerical study. Int. J. Rock Mech. Min. Sci. 41, 1191–1210. http://dx.doi.org/10.1016/j.ijrmms.2004.05.005.

Mitchell, T.M., Faulkner, D.R., 2012. Towards quantifying the matrix permeability of fault damage zones in low porosity rocks. Earth Planet. Sci. Lett. 339–340, 24–31. http://dx.doi.org/10.1016/j.epsl.2012.05.014.

Mitchell, T.M., Faulkner, D.R., 2009. The nature and origin of off-fault damage surrounding strike-slip fault zones with a wide range of displacements: a field study from the Atacama fault system, northern Chile. J. Struct. Geol. 31, 802–816. http://dx.doi.org/10.1016/j.jsg.2009.05.002.

Mohanty, S., Hsiung, S., 2011. An Experimental Investigation of Single Fracture Behaviorunder Normal and Shear Loads.

Nara, Y., Koike, K., Yoneda, T., Kaneko, K., 2006. Relation between subcritical crack growth behavior and crack paths in granite. Int. J. Rock Mech. Min. Sci. 43, 1256–1261. http://dx.doi.org/10.1016/j.ijrmms.2006.03.016.

Nara, Y., Meredith, P., Mitchell, T., 2013. Influence of macro-fractures and fault gouge on permeability in basalt. In: EGU General Assembly 2013, Held 7-12 April, 2013 in Vienna, Austria, Id. EGU2013-1493, pp. 2013.

Nara, Y., Meredith, P.G., Yoneda, T., Kaneko, K., 2011. Influence of macro-fractures and micro-fractures on permeability and elastic wave velocities in basalt at elevated pressure. Tectonophysics 503, 52–59. http://dx.doi.org/10.1016/j.tecto.2010.09.027.

Neuzil, C.E., 1995. Abnormal oressures as hydrodynamic phenomena. Am. J. Sci. 295, 742–786.

Nishiyama, S., Ohnishi, Y., Ito, H., Yano, T., 2014. Mechanical and hydraulic behavior of a rock fracture under shear deformation. Earth, Planets Sp. 66, 108. http://dx.doi.org/10.1186/1880-5981-66-108.

Olsson, R., Barton, N., 2001. An improved model for hydromechanical coupling during shearing of rock joints. Int. J. Rock Mech. Min. Sci. 38, 317–329. http://dx.doi.org/10.1016/S1365-1609(00)00079-4.

Olsson, W.A., Brown, S.R., 1993. Hydromechanical response of a fracture undergoing compression and shear. Int. J. Rock Mech. Min. Sci. 30, 845–851. http://dx.doi.org/10.1016/0148-9062(93)90034-B.

Pérez-Flores, P., Cembrano, J., Sanchez, P., Veloso, E., Arancibia, G., Roquer, T., 2016. Tectonics, magmatism and paleo-fluid distribution in a strike-slip setting: insights from the northern termination of the Liquiñe-Ofqui fault System, Chile. Tectonophysics 680, 192–210. http://dx.doi.org/10.1016/j.tecto.2016.05.016.

Persson, B.N.J., Albohr, O., Tartaglino, U., Volokitin, A.I., Tosatti, E., 2005. On the nature of surface roughness with application to contact mechanics, sealing, rubber friction and adhesion. J. Phys. Condens. Matter 17, R1–R62. http://dx.doi.org/10.1088/0953-8984/17/1/R01.

Power, W.L., Tullis, T.E., 1991. Euclidean and fractal models for the description of rock surface roughness. J. Geophys. Res. 96, 415. http://dx.doi.org/10.1029/90JB02107.

Radic, J.P., 2010. Las cuencas cenozoicas y su control en el volcanismo de los Complejos Nevados de Chillán y Copahue-Callaqui (Andes del Sur, 36-39 ° S). Andean Geol. 37, 220–246.

Raven, K.G., Gale, J.E., 1985. Water flow in a natural rock fracture as a function of stress and sample size. Int. J. Rock Mech. Min. Sci. 22, 251–261. http://dx.doi.org/10.1016/0148-9062(85)92952-3.

Roquer, T., Arancibia, G., Rowland, J., Iturrieta, P., Morata, D., Cembrano, J., 2017. Fault-controlled development of shallow hydrothermal systems: structural and mineralogical insights from the Southern Andes. Geothermics 66, 156–173. http://dx.doi.org/10.1016/j.geothermics.2016.12.003.

Rosenau, M., Melnick, D., Echtler, H., 2006. Kinematic constraints on intra-arc shear and strain partitioning in the southern Andes between 38 ° S and 42 ° S latitude. Tectonics 25, 1–16. http://dx.doi.org/10.1029/2005TC001943.

Rowland, J.V., Sibson, R.H., 2004. Structural controls on hydrothermal flow in a segmented rift system, Taupo Volcanic Zone, New Zealand. Geofluids 4, 259–283. http://dx.doi.org/10.1111/j.1468-8123.2004.00091.x.

Sagy, A., Brodsky, E.E., Axen, G.J., 2007. Evolution of fault-surface roughness with slip. Geology 35, 283–286. http://dx.doi.org/10.1130/G23235A.1.

Sanchez-Alfaro, P., Reich, M., Arancibia, G., Pérez-Flores, P., Cembrano, J., Driesner, T., Lizama, M., Rowland, J., Morata, D., Heinrich, C.C.A., Tardani, D., Campos, E., 2016. Physical, chemical and mineralogical evolution of the Tolhuaca geothermal system, southern Andes, Chile: insights into the interplay between hydrothermal alteration and brittle deformation. J. Volcanol. Geotherm. Res. 324, 88–104. http://dx.doi.org/10.1016/j.jvolgeores.2016.05.009.

Sánchez, P., Pérez-Flores, P., Reich, M., Arancibia, G., Cembrano, J., 2013. Crustal deformation effects on the chemical evolution of geothermal systems: the intra-arc Liquiñe–Ofqui Fault System, Southern Andes. Int. Geol. Rev. 55, 37–41. http://dx.doi.org/10.1080/00206814.2013.775731.

Scholz, C.H., Gupta, A., 2000. Fault interactions and seismic hazard. J. Geodyn. 29, 459–467.

Sibson, R.H., 1996. Structural permeability of fluid-driven fault-fracture meshes. J. Struct. Geol. 18, 1031–1042. http://dx.doi.org/10.1016/0191-8141(96)00032-6.

Sielfeld, G., Cembrano, J., Lara, L., 2016. Transtension driving volcano-edifice anatomy: insights from Andean transverse-to-the-orogen tectonic domains. Quat. Int. 1–17. http://dx.doi.org/10.1016/j.quaint.2016.01.002.

Song, I., Elphick, S.C., Main, I.G., Ngwenya, B.T., Odling, N.W., Smyth, N.F., 2004. One-dimensional fluid diffusion induced by constant-rate flow injection: theoretical analysis and application to the determination of fluid permeability and specific storage of a cored rock sample. J. Geophys. Res. Solid Earth 109, 1–13. http://dx.doi.org/10.1029/2003JB002395.

Stanton-Yonge, A., Griffith, W.A., Cembrano, J., St. Julien, R., Iturrieta, P., 2016. Tectonic role of margin-parallel and margin-transverse faults during oblique subduction in the Southern volcanic zone of the Andes: insights from boundary element modeling. Tectonics 1–24. http://dx.doi.org/10.1002/2016TC004226.

Suárez, M., Emparan, C., 1997. In: Servicio, N. (Ed.), Hoja Curacautín, región de la Araucanía y del Biobío. Carta Geológica de Chile, Servicio Nacional de Geología y Minería.

Talwani, P., Acree, S., 1985. Pore pressure diffusion and the mechanism of reservoir-induced seismicity. Pure Appl. Geophys. 122, 947–965.

Tardani, D., Reich, M., Roulleau, E., Takahata, N., Sano, Y., Pérez-Flores, P., Sánchez, P., Cembrano, J., Arancibia, G., Sánchez-Alfaro, P., Cembrano, J., Arancibia, G., Sa, P., Sano, Y., Pe, P., Arancibia, G., 2016. Exploring the structural controls on helium, nitrogen and carbon isotope signatures in hydrothermal fluids along an intra-arc fault system. Geochim. Cosmochim. Acta 184, 193–211. http://dx.doi.org/10.1016/j.gca.2016.04.031.

Turcotte, D.L., 1992. Fractals and Chaos in Geology and Geophysics. Cambridge University Press.

Uehara, S. ichi, Shimamoto, T., 2004. Gas permeability evolution of cataclasite and fault gouge in triaxial compression and implications for changes in fault-zone permeability structure through the earthquake cycle. Tectonophysics 378, 183–195. http://dx.doi.org/10.1016/j.tecto.2003.09.007.

Veloso, E.E., Anma, R., Yamaji, A., 2009. Ophiolite emplacement and the effects of the subduction of the active Chile ridge System: heterogeneous paleostress regimes recorded in the Taitao Ophiolite (Southern Chile). Andean Geol. 36, 3–16. http://dx.doi.org/10.5027/andgeoV36n1-a01.

Vicencio, V., 2015. Geología y mineralogía de alteración en una sucesión volcano-sedimentaria en la Zona Volcánica Sur Central, Chile. Evidencias de un paleo-sistema volcánico y geotermal en la Formación Cura-Mallín Universidad de Chile.

Walker, R.J., Holdsworth, R.E., Armitage, P.J., Faulkner, D.R., 2013. Fault zone permeability structure evolution in basalts. Geology 41, 59–62. http://dx.doi.org/10.1130/G33508.1.

Walsh, J.B., Grosenbaugh, M.A., 1979. A New model for analyzing the effect of fractures on compressibility. J. Geophys. Res. 84.

Wang, G., Mitchell, T.M., Meredith, P.G., Nara, Y., Wu, Z., 2016. Influence of gouge thickness and grain size on permeability of macro-fractured basalt. J. Geophys. Res. Solid Earth. http://dx.doi.org/10.1002/2016JB013363.

Watanabe, N., Hirano, N., Tsuchiya, N., 2008. Determination of aperture structure and fluid flow in a rock fracture by high-resolution numerical modeling on the basis of a flow-through experiment under confining pressure. Water Resour. Res. 44, 1–11. http://dx.doi.org/10.1029/2006WR005411.

Whitney, D.L., Evans, B.W., 2010. Abbreviations for names of rock-forming minerals. Am. Mineral. 95, 185–187. http://dx.doi.org/10.2138/am.2010.3371.

Wibberley, C. a., Shimamoto, T., 2003. Internal structure and permeability of major strike-slip fault zones: the median tectonic line in Mie prefecture, Southwest Japan. J. Struct. Geol. 25, 59–78. http://dx.doi.org/10.1016/S0191-8141(02)00014-7.

Witherspoon, P.A., Wang, J.S.Y., Iwai, K., Gale, J.E., 1980. Validity of Cubic Law for fluid

flow in a deformable rock fracture. Water Resour. Res. 16, 1016–1024. http://dx.doi.org/10.1029/WR016i006p01016.

Zhang, S., Tullis, T.E., 1998. The effect of fault slip on permeability and permeability anisotropy in quartz gouge. Tectonophysics 295, 41–52. http://dx.doi.org/10.1016/S0040-1951(98)00114-0.

Zhang, Y., Schaubs, P.M., Zhao, C., Ord, A., Hobbs, B.E., Barnicoat, A.C., 2008. Fault-related dilation, permeability enhancement, fluid flow and mineral precipitation patterns: numerical models. Geol. Soc. Lond. Spec. Publ. 299, 239–255. http://dx.doi.org/10.1144/SP299.15.

Zimmerman, R.W., 2012. The History and Role of the Cubic Law for Fluid Flow in Fractured Rocks. Agu 2012 Presentation.

Zucchi, M., Brogi, A., Liotta, D., Rimondi, V., Ruggieri, G., Montegrossi, G., Caggianelli, A., Dini, A., 2017. Permeability and hydraulic conductivity of faulted micaschist in the eastern Elba Island exhumed geothermal system (Tyrrhenian sea, Italy): insights from Cala Stagnone. Geothermics 70, 125–145. http://dx.doi.org/10.1016/j.geothermics.2017.05.007.